

Chapter 2

Wind Waves and the Mechanisms of Air-Sea Transfer

One outstanding lesson of the previous chapter is that wind waves play a central role in air-sea transfer processes. In this chapter, we examine how wind waves first arise on a wind-blown water surface, what laws govern their growth, what processes are responsible for their decay, and how exactly they facilitate the transfer of momentum and of scalar properties across the air-sea interface.

2.1 The Origin of Wind Waves

In a triumph of early twentieth century fluid mechanics, a combination of theory and laboratory experiment elucidated the origin of turbulence, as Schlichting (1960) has authoritatively chronicled. The theoretical advance was the development of stability theory for laminar shear flow in a boundary layer, with the “Orr-Sommerfeld Equation” (OSE) as its centerpiece and principal tool for analytical investigations. This equation describes the behavior of small-amplitude wave-like disturbances on laminar shear flow that spontaneously grow to large amplitude (“instability waves”). Instability waves in laminar boundary layer flow became known as “Tollmien-Schlichting waves,” after the theoreticians who explored their properties.

For some time, such waves eluded efforts at observing them in the laboratory, because laminar flow free of residual turbulence is almost impossible to maintain. Finally, in a wind tunnel made painstakingly clear of other disturbances, the *experimentum crucium* of Schubauer and Skramstad (1947) demonstrated that Tollmien-Schlichting waves of highest theoretical growth rate were the initially observed surface undulations. This verified the theory on the supposition that minute random disturbances of all other wavelengths were present from the beginning, but only the most unstable

ones grew to an observable amplitude. The theoretically predicted exponential growth for the instability waves also meant that they would rapidly outgrow the small amplitude assumption. Indeed, laboratory Tollmien-Schlichting waves soon break down into chaotic motions and eventually into full-blown turbulence.

A similar story unfolded in the second half of the century about the origin of wind waves, which we will take to mean the first appearance of small-amplitude waves on an initially smooth water surface under suddenly arising wind. This had remained an enigma in spite of numerous attempts at explanation. Ursell (1956) wrote in a review of the subject: "Wind blowing over a water surface generates waves in the water by physical processes which cannot be regarded as known."

In his book, Phillips (1977) gives a full account of two later theories attempting to explain wave generation: one his own theory that holds pressure fluctuations in the turbulent wind responsible, and two, the theory developed by Miles (1957, 1959, 1962) and Brooke-Benjamin (1959, 1960), that attributes wave growth to coupling between waves and a "critical" layer in the air flow where the wind speed equals wave celerity. The latter theory has attracted a great deal of attention. It concentrates on the air side, ignores shear flow on the water side, and treats viscous effects approximately, if at all taking them into account. In light of later evidence, the most damaging overidealization of this theory was failing to apply the full set of four interface boundary conditions, relying on ad-hoc approximations instead. The Miles-Brooke Benjamin theory nevertheless gave much insight into the dynamics of the air flow over a wavy interface, even if it explains neither the first appearance of waves on an initially smooth surface upon sudden wind, nor the later growth of waves from moderate to larger height.

As in the case of turbulence, the theoretical explanation of wind wave origin finally came from the Orr-Sommerfeld equation supported by laboratory experiment. The theory was more complicated than in the case of turbulence near a solid boundary, because it had to take full account of shear flow both in the air and in the water, as well as of four interface boundary conditions. The latter require continuous normal and tangential velocity and shear stress, and surface pressures in air and water differing on account of surface tension. Wuest (1949) first formulated the stability problem in these terms (originally in a doctoral thesis dated 1941), followed later independently by Lock (1953). Wuest calculated instability waves on some overidealized basic flows and demonstrated the essential importance of satisfying all four interface conditions. Lock took the undisturbed shear flow velocity distribution to be laminar on both sides of the interface, and discovered "air-side" and "water-side" waves with different stability properties. The air-side wave motions were much like Tollmien-Schlichting waves that only induced small amplitude oscillations on the water surface. The water-side wave motions in the shear flow engendered larger surface displacements and traveled at a speed close to the propagation speed of free surface waves on stagnant water. Lock's (1953) study anticipated later work, but lack of observational evidence left it in limbo for years.

The first observations of wave growth under sudden wind, in a laboratory flume (wind tunnel over a water channel), came a quarter of a century later, with the aid of the microwave backscatter technique that enables satellites to observe the ocean

surface (Larson and Wright, 1975). After a sudden start, the air flow became fully turbulent in the first second, so that no air-side instability waves could be observed. On the water surface, however, regular short waves appeared spontaneously, their amplitude increasing for some ten seconds before breaking down into irregular motions. The experimental technique yielded the growth rate of individual spectral components of surface elevation. The spectral densities grew exponentially, indicating instability waves. The wavelengths observed were quite short, close to the wavelength of capillary-gravity waves of minimum speed, which is about 1.7 cm. Theoretical growth rates in the same wavelength range were then calculated by Valenzuela (1976) from the Orr-Sommerfeld equation with all four interface conditions. He found encouraging agreement between theory and observation, although the lack of information on the velocity distribution in the Larson and Wright (1975) experiment made the application of the stability theory somewhat uncertain.

The comprehensive laboratory and theoretical investigation of Kawai (1979) fully established the agreement of theory and observation. In his seminal paper, Kawai described how waves develop on an initially smooth surface, upon turning on the air flow in a laboratory flume: “A shear flow first starts and grows in the uppermost thin layer of the water, and then the appearance of waves follows several seconds later. The waves that appear initially are long-crested and regular, and so they are distinguished from those appearing later, which are short-crested, irregular, and accompanied by forced convection.” By forced convection, Kawai means turbulence in the water; short-crested, irregular waves are laboratory wind waves. The initial period during which the waves were long-crested and regular lasted some ten seconds.

Kawai also calculated the growth rates of the waves over the range of wavelengths observed, from the OSE with the full set of four boundary conditions. He used the observed laminar shear flow profile in the water, and an empirical turbulent velocity distribution in the air. As Schubauer and Skramstad thirty odd years before, Kawai ended up by concluding that the observed “initial wavelets are the waves whose growth rate by the instability mechanism is maximum.”

A crucial aspect of the above scenario, as calculated or observed, is that when the initial regular waves break down into irregular wind waves, the water-side shear flow simultaneously breaks down into turbulence. The theoretical instability waves consist of wave-like motions in the air and in the water, as well as on the interface. When one of these interacting flow structures breaks down into chaotic motions, so must the others. Putting it another way, with the water side in mind, the water-side instability waves are the equivalents of Tollmien-Schlichting waves in laminar boundary layer flow, satisfying different boundary conditions, however. As these instability wave motions in the water break down, so do the regular surface waves associated with them. Clearly the shear flow, the unstable wave motions in the air and in the water, and the waves on the interface are all tightly coupled. There is every reason to expect this coupling to remain a characteristic of the flow after breakdown into turbulence and wind waves. Just as turbulence, wind waves are then the product and property of the air-sea shear flow.

2.1.1 Instability Theory

The origin of wind waves, according to the above story, is “explained” by instability theory. In order to accept the explanation, we must judge as realistic the idealizations the theory is built upon, know how its predictions are calculated, and be convinced of the theory’s correctness by the agreement of its predictions with observation. To be useful, a theory must also be, in Einstein’s words, “as simple as possible, but not simpler.”

The centerpiece of instability theory, the Orr-Sommerfeld equation, derives from the equations of motion, upon a set of idealizations (see e.g., Schlichting (1960)). From one point of view, it is a generalization of the classical theory of small amplitude free surface waves on a stagnant inviscid fluid, discussed at length in Lamb’s (1957) classical treatise on Hydrodynamics. As the classical theory, the derivation of the OSE postulates small-amplitude sinusoidal disturbances on a wind-blown water surface, of wavelength λ , wavenumber $k = 2\pi/\lambda$. In departures from classical theory, wave amplitude may grow or decay, and the wave motion coexists with two-dimensional parallel viscous shear flow in the (x, z) plane, both in the air and in the water, $U(z)$. “Small amplitude” means that particle velocities in the waves are much less than either the characteristic shear flow velocity or the wave propagation speed (“celerity”). The wave motions are then small perturbations on the mean flow, and linearized equations of motion and continuity describe their behavior. Instability waves necessarily outgrow the small amplitude assumption at some time: Breakdown into chaotic motions follows, but is outside the scope of the theory.

The theory portrays the instability wave motions by a streamfunction ψ , constant ψ lines paralleling the velocities, $u = \partial\psi/\partial z$, $w = -\partial\psi/\partial x$. The wave-like flow pattern propagates and intensifies or decays according to the relationship:

$$\psi = \phi(z) \exp \{ik(x - ct)\} \quad (2.1)$$

where $\phi(z)$ is the amplitude of the streamfunction, and the celerity $c = c_r + ic_i$ is complex, the real part being the propagation speed of the waves, the imaginary part portraying wave growth at the rate of kc_i . The equations of motion and continuity now require the amplitude of the instability waves to obey the following equation, primes meaning differentiation with respect to z :

$$(U - c)(\phi'' - k^2\phi) + U''\phi = -ivk^{-1}(\phi'''' - 2k^2\phi'' + k^4\phi) \quad (2.2)$$

known as the Orr-Sommerfeld equation. In the case of the air-water shear flow, the equation applies separately to the air and to the water, the solutions depending on the different viscosities. Boundary conditions at “infinity” (i.e., high above and deep below the interface) are that both velocity components u , w vanish. The equation is of fourth order, requiring four boundary conditions in the air, and four in the water, for a total of eight – two plus two as mentioned at plus-minus infinity, as well as four matching conditions at the interface, prescribed by the dynamics of viscous fluids.

They are: continuity of the two velocity components u , w ; of the shear stress τ ; and a pressure condition expressing the balance between the air-water pressure difference and the force arising from surface tension on the curved interface. Simplified forms of these conditions apply to the postulated small perturbations – they are listed in a number of publications, including Kawai (1979).

The simplified shear stress and pressure conditions at the interface are still quite complex, and so is the OSE itself for that matter, containing the velocity distribution and its second derivative. Analytical discussions of the OSE with these boundary conditions have not been very illuminating. Numerical solutions of Valenzuela (1976), Kawai (1979), and others have, however, led to important insights into mechanism of instability and revealed the properties of instability waves on the air-sea interface.

The usual numerical procedure starts with asymptotic solutions of Equation 2.2, for fixed wavenumber, at large distances above and below the interface, where U'' vanishes, and U is constant. Two such solutions exist on each side of the interface, one like the classical inviscid wave, the other rapidly varying with height or depth, known as the “viscous solution.” Starting with these well above and well below the interface, with their amplitudes arbitrarily set at unity, the integration proceeds “top down” and “bottom up.” Arriving at the interface, one has then two inviscid and two viscous solutions, with four calculated amplitudes, which have to satisfy four boundary conditions. The determinant of the resulting four homogeneous linear equations has to vanish, a condition yielding the complex celerity $c_r + ic_i$. The three remaining equations yield the amplitude ratios of the four solutions.

There are various practical problems in carrying out the integrations and in solving the four equations that arise from the interface boundary conditions. These are dealt with by different ingenious methods. As may be expected, the results depend on the assumed air flow and water flow velocity distributions. The solutions reveal exponentially growing waves over a limited range of wavenumbers – their growth rate peaks at some wavenumber k_m . If initial waves appearing under sudden wind have this wavenumber, then we take it for granted that they arise from shear flow instability.

The various simplification of the theory, consisting of the OSE and the boundary conditions, make it “as simple as possible,” for the understanding of instability waves on the air-water shear flow. Let us now make it simpler, by neglecting viscosity, and eliminating the shear flow, $U = 0$. The remaining simple equation has the solution $\phi = \text{const.} \exp(\pm kz)$, and describes the classical inviscid wave. It neither grows nor decays, and its celerity is real, given by:

$$c^2 = k\gamma + \frac{g}{k} \quad (2.3)$$

which is the classical “dispersion” relationship (because waves of different wavelengths “disperse,” i.e., travel at different speeds) valid for small amplitude waves on stagnant water. At high wavenumbers the first term on the right dominates: These are

capillary waves, in contrast to gravity waves at low k . The celerity is real, waves of given wavelength travel at constant speed c and constant amplitude ϕ_w/c . The wave speed has a minimum at wavenumber $k = \sqrt{g/\gamma}$, where $c^2 = 2\sqrt{g\gamma}$.

Simplification led us to the classical theory of gravity-capillary wave propagation on the surface of a stagnant fluid, from the theory of instability waves growing on shear flow. Reversing the argument, we see that the full four boundary condition instability wave theory may be regarded as an extension of the classical theory of surface waves on water. In this light, Lock's result, that the water-side instability waves travel at much the same speed as inviscid surface waves, is not so surprising.

2.1.2 Properties of Instability Waves

A realistic specification of the mean shear flow profiles in air and water was one of the key factors in Kawai's (1979) success in reconciling theory and experiment. As mentioned before, in laboratory flumes the air flow is turbulent immediately upon starting (in the first second, at any rate, according to Larson and Wright, 1975), but the water-side shear flow remains laminar for several seconds. Kawai therefore chose an empirical turbulent air flow velocity distribution, together with a laminar shear flow profile in the water, fitted to the actual observed velocity distribution. His air flow observations did not cover the velocity distribution over that portion of the water surface where the initial waves appeared – the empirical distribution he used had two parameters, the air-side friction velocity u_a^* , and nominal wind speed, U_1 . Observation yielded the friction velocity, but the nominal wind speed was uncertain with an estimated possible range of $U_1 = 5u_a^*$ to $8u_a^*$.

Numerical solution of the OSE yielded frequencies, phase speeds, and growth rates of waves of different wavelengths, at the observed friction velocities, for the two nominal air flow speeds bracketing the range of uncertainty. The phase speeds differed little from what the classical dispersion relationship predicts, indicating that they are little affected by viscosity or shear flow. Kawai (1979) showed the frequency $f = k_m c_r / 2\pi$ and growth rate $\beta = 2 k_m c_i$ of the waves with the highest calculated growth rate, together with the observed frequency and growth rate of the initial wavelets, in two dramatic illustrations (see Figures 2.1a and b). The dashed lines represent calculated quantities at the two nominal air speeds, the different circular symbols the experimental results. The agreement of theory and observation is striking, given the great difficulty of both.

Kawai's (1979) maximum growth rates are fairly high and the initial wavelets have wavelengths close to those of capillary-gravity waves of minimum celerity, in the wavenumber range of $2\text{--}5 \text{ cm}^{-1}$, similarly to what Larson and Wright (1975) found. This raised the intriguing question: Is there some physical mechanism holding the most unstable waves at this singular point of the gravity-capillary wave dispersion relationship? Numerical solutions of the OSE (Wheless and Csanady, 1993), in a range of wavenumbers around those of Kawai (1979) and of Larson and Wright (1975), $k = 1\text{--}8 \text{ cm}^{-1}$, proved otherwise. The growth rate of the instability waves turned out to be sensitive to the "development time" t_d of the laminar boundary layer in

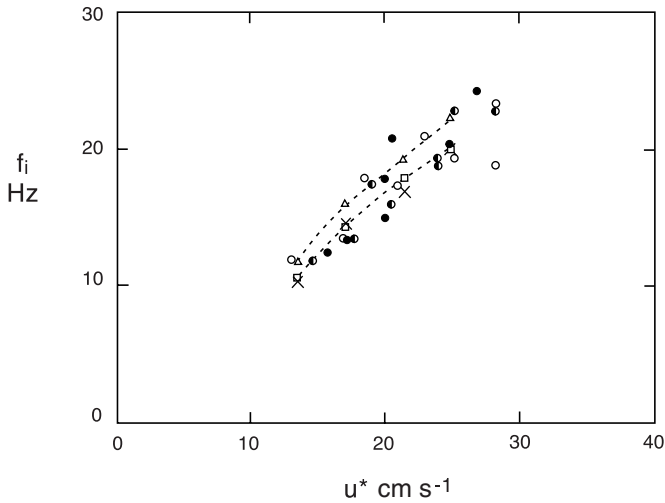


Figure 2.1a Frequency f_i of the observed initial wavelets in Kawai's experiments at fetches of 3 to 8 meters (full, half-open and open circles) versus friction velocity. Calculated growth rates (squares and triangles) are connected by dotted lines, bracketing the realistic range of U_1/u^* ratios, ranging from 5 to 8.

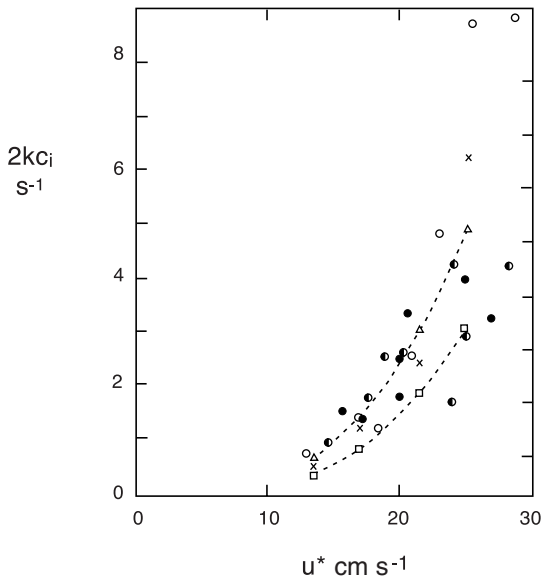


Figure 2.1b Energy growth rate of the observed initial wavelets and calculated values in Kawai's experiments. Symbols and dotted lines as in previous figure.

the water (time since starting the air flow). With increasing development time, the water-side boundary layer depth grew as $\delta = \sqrt{2\nu_w t_d}$, and the inverse wavenumber of the most unstable wave grew in proportion, approximately as $k_m^{-1} = 0.97\delta$ (Figure 2.1c). Given that laboratory observation of initial wavelets is restricted to

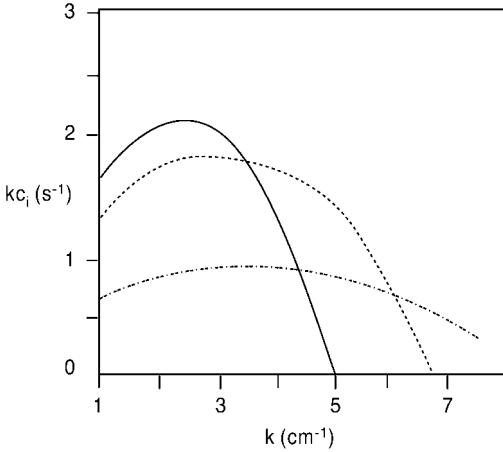


Figure 2.1c Calculated growth rate of instability waves against wavenumber, at varying thickness of the water-side viscous boundary layer. The growth rate peaks at a wavenumber k_p varying as the inverse of the boundary layer thickness δ , $k_p^{-1} = 1.35\delta$. From Wheless and Csanady (1993).

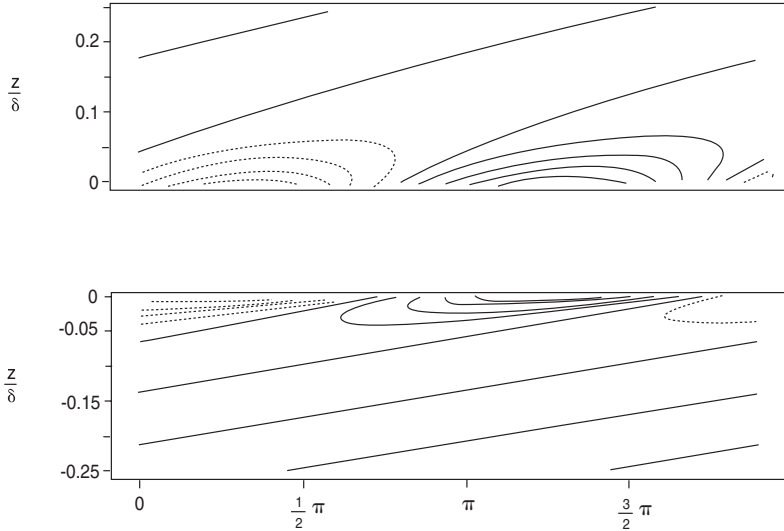


Figure 2.1d Streamlines of the instability wave of the highest growth rate on the two sides of the air-sea interface. Significant motion is confined to about $z/\delta < 0.05$, or about one millimeter from the interface. From Wheless and Csanady (1993).

development times of some 3 to 10 seconds, and that the viscosity of water is nearly constant at $\nu_w = 0.01 \text{ cm}^2 \text{ s}^{-1}$, the observable range of k_m has to fall between 2 and 4.2 cm^{-1} , as observations indeed showed.

Calculations also revealed the structure of the instability waves, the outstanding characteristic of which is a dense packing of streamlines on both the air and the water side, signifying high horizontal velocities (Figure 2.1d). This arises from the “viscous solution” of the OSE, the component that ensures continuity of shear stress and horizontal velocity across the interface. Lock (1953) has already drawn attention to

such a viscous-wave boundary layer. Its thickness is typically a quarter of a millimeter, and its effect on the velocity distribution is to increase surface velocity in the water by about an order of magnitude, compared to the surface velocity in an inviscid free wave of the same wavelength and amplitude. This means that an instability wave outgrows the small amplitude assumption at very low amplitude, leading to early breakdown of the flow into irregular motions. The vorticity is high in the viscous-wave boundary layer: The initial wavelets thus harbor incipient eddies, which remain to contribute to the irregular motions. A final point is that the energy transfer from the mean flow to the wave motion (the product of shear stress and rate of strain) peaks in the *air-side* viscous-wave boundary layer, where the streamlines are close together and the velocity gradient is large (not in the “critical” layer).

While the laboratory experiments in which instability waves arise on a quiescent water surface under sudden wind seem remote from oceanic reality, something very similar does occur under a wind gust. The “cat’s paws” of everyday experience are patches of sea surface covered by capillary-gravity waves, looking for all the world like the initial waves in Kawai’s laboratory flume. It is eminently reasonable to suppose that they arise from the same causes, wind-driven surface shear and hydrodynamic instability. Within seconds they evolve into the irregular surface typical of wind waves, containing also somewhat longer waves. As the gust passes (after a typical duration of perhaps 100 seconds), the shortest waves die out until the next such episode. Each gust generates a new boundary layer at the surface, thin and strongly sheared, setting the stage for new instability waves to grow. This is not mere speculation: There can be no doubt that a wind gust greatly intensifies surface shear, nor that such a shear layer is hydrodynamically unstable. If instability waves in the gravity-capillary range occur under similar conditions in the laboratory, they can hardly fail to show up on a natural water surface. Nor can there be any doubt that turbulence generation in the water accompanies the evolution of initial wavelets into chaotic surface waves, as the highly vortical water-side instability waves break down. Thus, the natural variability of turbulent air flow over water brings about incessant generation and decay of short, steep wavelets.

2.2 The Wind Wave Phenomenon

The wind waves we encounter in nature are much higher and longer than cat’s paws and their laboratory cousins arising from instability waves. What the instability theory and accompanying laboratory work has shown is that short waves arise spontaneously on the interface, and break down into irregular surface motions simultaneously with the generation of turbulent shear flow. A bold generalization of this finding is a modern view of wind waves, first articulated in recent writings of Professor Toba of Tohoku University, to the effect that the wind-blown high waves of the ocean are a complement of the air-sea turbulent shear flow from which they cannot be separated. He puts it this way (Toba, 1988):

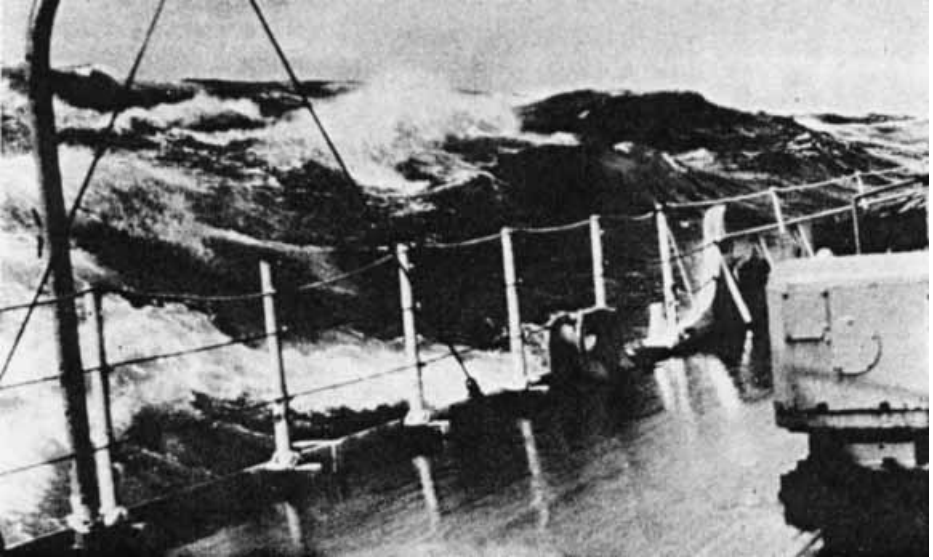


Figure 2.2 The windsea in a condition described by the U.S. Coast Guard as “moderately high and breaking,” photographed from ship. From Bigelow and Edmonson (1947).

“The wind wave is a special water wave as it is generated by the action of wind at the air-water interface. Since the wind wave is associated with air and water flows above and below the waves, its characteristics are determined by the coupling process between the boundary layers in air and water. The important elements in the wind wave are the surface wave motion, the local wind-drift and turbulence in the air and water boundary layers” (p. 263).

A precursor of the new paradigm appears in older nautical texts as a distinction between “sea” and “swell,” the former meaning the irregular and rapidly changing sea surface under moderate to strong winds, the latter the smooth, regular waves propagating from some distant generation region to the observer’s location. Bigelow and Edmondson (1947) describe the distinction as follows: “The characteristics of storm waves that most impress the observer are their irregularity and steepness, also their great heights in many cases, and the frequency with which their crests break.” They show two Coast Guard photographs in illustration (Figure 2.2 is one of them). They then continue: “the shapes of the waves undergo wide alterations when the wind dies down, or when the waves produced by a given wind system advance to regions outside the latter, as very commonly happens. The wave train in question is then known as a ‘swell’ . . .” characterized by low, rounded crests and smooth surface contours. When the wind dies, the waves begin to lose energy, “the shorter ones with the least energy becoming lower and disappearing first, so that the longer ones alone are left. At the same time, the sharp peaks so frequent during a rough sea subside,” the irregularities of the surface smooth out, “and the remaining crests decrease progressively in height and become more rounded. The end result is that the waves tend to approach the trochoidal profile characteristic of the so-called free wave of theory.”

Toba's view quoted above ascribes the special character of wind waves to close coupling with the air-water shear flow. It conflicts with the earlier conceptual model of wind waves, that regarded them an assembly of freely propagating gravity waves, independent of and unaffected by the air-water shear flow. The new conceptual model holds the irregular wind-blown water surface to be just one manifestation of the complex coupling between air and water turbulent shear flow. A newly coined, felicitously descriptive term for the wind wave phenomenon is "windsea."

Because the wind generates both the windsea and the turbulent shear flow, the independence of the two wind products is inherently improbable. Where there is no wind, shear flow and turbulence are also absent. Any waves in such regions are smooth and more or less regular, so that they are legitimately regarded as free gravity waves, swell for short. As may be expected, in the ocean windsea and swell appear together more often than not. Properties of the windsea emerge from observations under steady winds, in the absence of swell (i.e., under rather special conditions).

Casual observation of the windsea under such conditions from ship, sailing boat, pier, or beach readily identifies "dominant" waves propagating downwind, with more or less parallel crests, more or less evenly spaced, of more or less the same height (all of these with wide error bars), together with much irregularity. The dominant waves have an identifiable mean wavelength; moreover, they propagate at a speed close to the phase speed of the classical inviscid wave of that wavelength. This is easily verified at sea, under the right conditions: one observation I can attest to, made hundreds of kilometers from shore, from a cruise ship traveling at 20 knots (10 m s^{-1}), in a tail wind blowing fortuitously at the same speed, showed dominant waves traveling together with the ship, and to have a wavelength λ (estimated using the ship as a length scale) of about 60 m. The observed wavelength approximately satisfies the gravity wave formula from equation 2.3, $k = 2\pi/\lambda = g/c^2$.

Dominant waves are not always this long, and they do not always travel at the speed of the wind. Anybody living along the shores of a large body of water has observed that dominant waves under wind blowing from the land are short, of small amplitude and of low celerity (speed of propagation). At increasing distances from shore, at longer "fetch" as this is called, the waves become both longer and higher. At some long enough distance, measured in hundreds of kilometers, the waves reach a fully developed or saturated stage. The dominant wave example of the last paragraph belongs to this stage.

Very different from the dominant waves are a great many short-scale surface disturbances of a wind-blown surface evident on casual observation. Structures of crescentic shape, in particular, of some 20 cm radius, with sharp fronts and broad backs, with a few capillary waves ahead of the front, are ubiquitous in a moderate wind, as any swimmer or sailor may easily observe. In stronger winds, bore-like fronts, of crest lengths of the order of meters, are added to the small-scale confusion, as well as many whitecaps generated by breaking long waves as seen in Figure 2.2. Looking into sunglint under a stiff breeze one sees something akin to President Bush's "myriad points of light": Like photographer's flashes, they light up for an instant and they

are gone. Presumably they are reflections from sharp fronts of short waves or bores, presumably curved, because the flashes seem to originate from point-like sources. Over a larger area, the many flashes give the impression of perpetual motion, somewhat like a TV screen that lost its signal. In a “slick” (band of smooth surface caused by a surface film of organic material) the flashes are absent. Cat’s paws, groups of capillary-gravity waves under a wind gust, indicate areas of locally high shear stress, and stand out in sunglint in moderate winds. In strong winds, the points of light in a sunglint apparently fuse together, and the water surface looks more like a very bright mirror.

The short surface structures are ephemeral, and their motions seem to be confined to a thin, vigorously stirred surface layer. Near Bermuda in the North Atlantic long straight rows of sargassum weed are visible from ships. Beneath the busy surface and the stirred layer, they remain apparently undisturbed as close to the surface as 0.1 m. The short and long waves clearly behave quite differently, as if they were different species; we will have to deal with their properties separately.

2.2.1 Wave Measures

First, we will discuss the long waves. Surface elevation in wind waves is an irregular function of time at a fixed location, of location at fixed time. Most of our wave observations come from instruments recording sea surface elevation above its equilibrium level, as a time series at a fixed location, $\zeta(t)$. Under steady conditions, this yields a stationary random process, analogous to the velocity record in turbulent flow that is steady in the mean. The root-mean-square elevation, $\sqrt{\overline{\zeta^2}}$, is one measure of wave height. An often used alternative measure is the average height, crest to trough, of the one-third highest waves, $H_{1/3}$. This is also known as the “significant wave height,” H_s . According to Longuet-Higgins (1952), quoted by Phillips (1977), for waves in the absence of swell a good approximation is $H_s = 4.0\sqrt{\overline{\zeta^2}}$.

An important characteristic of a stationary random process is its autocorrelation function, defined in this instance by $Z(t) = \overline{\zeta(t_0)\zeta(t_0 + t)}$, measuring over what time lag t surface elevations remain related. This is similar to autocorrelation functions we have met in the previous chapter, that define the size of eddies. An autocorrelation function of surface elevation in wind waves, observed in Chesapeake Bay, is shown in Figure 2.3, from Kinsman (1960), as quoted by Phillips (1977). Surface elevations remain related for a long time, as the slow decay of the successive peaks shows, but their sign changes rhythmically, signifying wave motion. The separation of the peaks defines the dominant period of the wave motion. An observer perceives dominant waves of much same period passing a fixed location. The envelope of the peaks decays on a time scale of some 5 periods, a measure of individual wave persistence. In casual observation, this comes across as groups of five or six extra high or extra low waves traveling together.

Another view of windsea properties emerges from another statistical measure, the frequency spectrum of surface elevation, $\phi(\omega)$, mathematically the Fourier transform

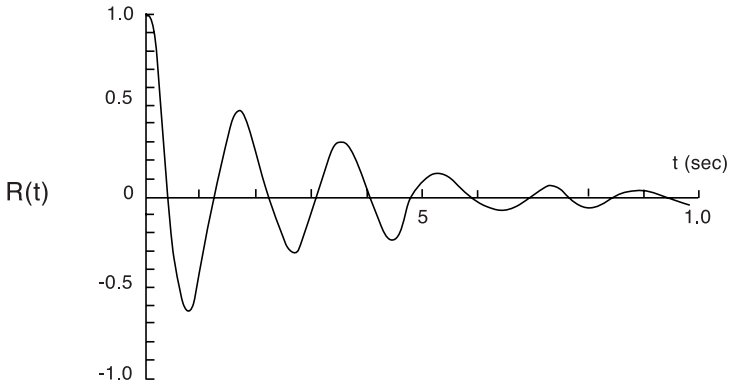


Figure 2.3 Autocorrelation function of surface elevation, observed at a location in Chesapeake Bay by Kinsman (1960), as quoted by Phillips (1977).

of the correlation function, with ω frequency in radians. Phillips (1977) defines the connection of these two functions as follows:

$$Z(t) = \int_0^{\infty} \phi(\omega) \cos(\omega t) dt$$

$$\phi(\omega) = \frac{2}{\pi} \int_0^{\infty} Z(t) \cos(\omega t) dt \quad (2.4)$$

$$\overline{\zeta^2} = \int_0^{\infty} \phi(\omega) d\omega.$$

According to the third equation, the frequency spectrum of wind waves describes contributions to mean square surface elevation, from Fourier components of different frequencies ω . Figure 2.4, from Pierson and Moskowitz (1964), shows observed spectra, obtained in steady winds of different speeds, far from any coasts. These characterize fully developed wind waves in the absence of swell. The spectrum has a single peak, and a relatively narrow spread around the peak, indicating that most of the contributions come from the dominant waves. Equations 2.4 imply that the frequency at the peak of the spectrum is close to the reciprocal of the dominant period gleaned from the correlation function, and that the width of the spectrum is inversely related to waveheight persistence.

With increasing wind speed, the peak of the spectrum becomes higher, and moves to lower frequency, but the character of the spectrum remains the same, single peak, narrow spread. This basic similarity suggests that statistical measures of wind waves, chaotic as the waves are, nevertheless may obey simple laws.

To discover such laws, if they exist, a logical approach is to find empirically what variables affect the spectrum, apply dimensional analysis, and see if the nondimensional relationships “collapse” to simple functions. What one hopes to find are empirical laws of physics akin to the transfer laws of the air-sea interface, characterizing now the behavior of the windsea.

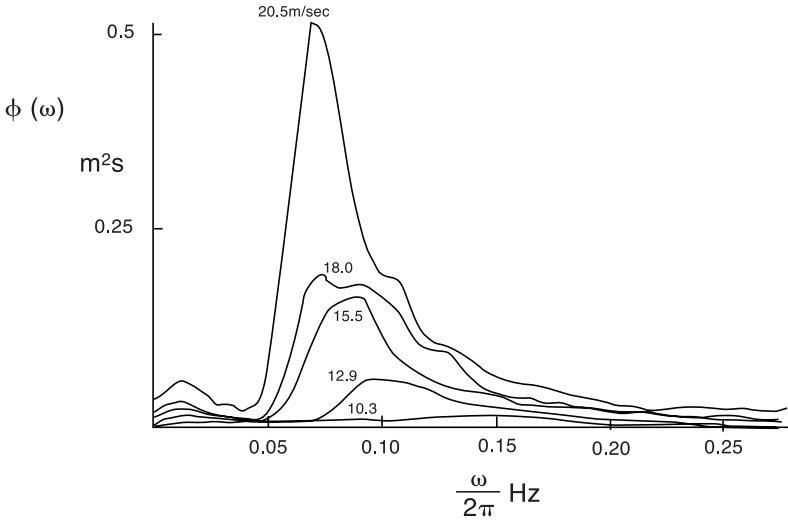


Figure 2.4 Frequency spectra of surface elevation for fully developed waves at different wind speeds, obtained by Pierson and Moskowitz (1964), as quoted by Kitagorodskii (1973).

Kitagorodskii (1973) carried out exactly this plan, relying on the Pierson-Moskowitz spectra for evidence. The observations showed that the spectral density $\phi(\omega)$ is a function of the ten-meter wind speed U , as well as of frequency ω . If, in the gravity wave range of the frequency, the only other variable of influence is the acceleration of gravity, g , the spectral density should obey a relationship of the form:

$$\phi(\omega) = \text{func.}(\omega, g, U) \quad (2.5)$$

or in nondimensional terms:

$$\frac{\phi(\omega)g^3}{U^5} = \text{func.}\left(\frac{\omega U}{g}\right). \quad (2.6)$$

Figure 2.5 is a replot of Figure 2.4 in these nondimensional variables, verifying the postulate of Equation 2.5. Kitagorodskii (1973) refers to this approach as similarity theory, and to the result, Equation 2.6, as a similarity law. He also notes that replacing the wind speed by the friction velocity u^* (related to $U(10)$ by Charnock's law of Chapter 1) leads to a physically more satisfactory relationship: It is the force of the wind, the wind stress, that directly drives the waves. The so-modified Equation 2.6 reveals u^* as the velocity scale of the wave motion in the windsea. That the same u^* is also the velocity scale of the shear flow and turbulence, is the strongest argument in support of the new paradigm that holds the windsea to be a byproduct of the turbulent shear flow in wind and water. We have already encountered the wind wave-turbulence connection in the transfer laws, where u^* scaled eddy velocities, while u^{*2}/g was a waveheight scale, as well as a roughness length characterizing the turbulent air flow.

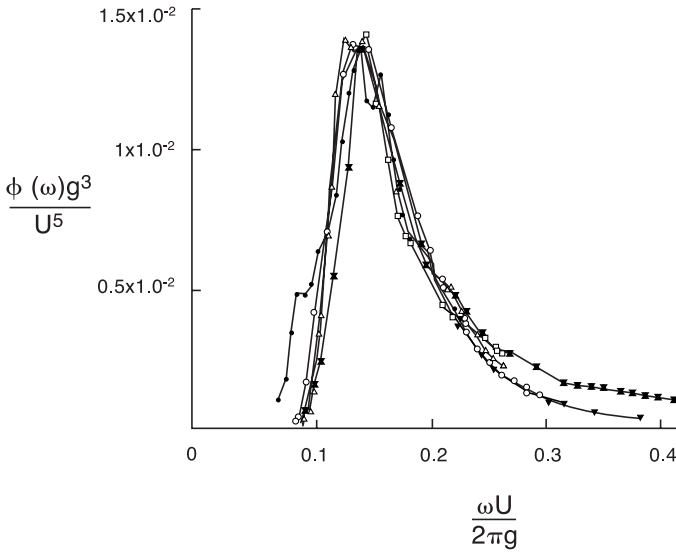


Figure 2.5 The frequency spectra of the previous figure plotted in nondimensional coordinates.

The nondimensional frequency of the spectral peak in Figure 2.5 is approximately $U\omega_p/g = 0.88$, and constitutes a key empirical characteristic of the “fully developed” windsea. Another such characteristic is the area under the spectrum, according to Equation 2.4 equal to $\overline{\zeta^2}$, the mean square surface elevation. The data yield $g\sqrt{\overline{\zeta^2}}/U^2 = 0.052$, a nondimensional measure of wave height. Taking a typical ratio $U/u^* = 27.5$, and replacing U by u^* in the formulae, Kitagorodskii’s similarity laws become, for wave height and peak frequency, in a fully developed windsea:

$$\frac{g\sqrt{\overline{\zeta^2}}}{u^{*2}} = 39.4 \quad (2.7)$$

$$\frac{u^*\omega_p}{g} = 0.032.$$

The relatively narrow spectrum with a single peak implies that the mean square elevation depends mainly on what we have so far called the “dominant” waves, having radian frequencies close to ω_p . These waves also propagate more or less at a phase speed given by the free gravity wave formula. The frequency at the peak of the spectrum then defines $C_p = g/\omega_p$, the celerity we may now assign to the characteristic wave, a precisely defined model of the dominant wave, of a frequency ω_p . According to the free gravity wave formula, the wavenumber is $k_p = g/C_p^2$, the wavelength $\lambda_p = 2\pi/k_p$ of the characteristic wave. Kitagorodskii’s similarity laws for fully developed waves give $C_p/u^* = 31$, or $C_p/U = 1.14$, the characteristic waves barely outrunning the 10 m wind. For the significant wave height $H_{1/3} = 4\sqrt{\overline{\zeta^2}}$, we find $gH_{1/3}/u^{*2} = 160$ and $gH_{1/3}/U^2 = 0.2$. These are very similar to rules of thumb summarized earlier by Stewart (1967).

2.2.2 Wave Growth

The above laws apply to wind waves far from coasts. Near a windward (upwind) coast, waves are short in wavelength and small in amplitude, in sharp contrast to their cousins far offshore. At increasing distances from the windward coast (at longer fetch), both wavelengths and wave heights increase, and the spectrum, at short distances confined to high frequencies, spreads to lower and lower frequency. Observation revealed that these changes also obey well-defined laws under constant wind stress and in the absence of swell. Under such conditions, statistical windsea properties depend on fetch, as well as on the variables in Equation 2.5. For the spectral density, the following extension of the similarity laws applies:

$$\phi = \text{func.}(u^*, g, \omega, X) \quad (2.8)$$

where X denotes fetch, the perpendicular distance from the upwind shore. The nondimensional version of this relationship is:

$$\frac{\phi g^3}{u^{*5}} = \text{func.}\left(\frac{u^* \omega}{g}, \frac{gX}{u^{*2}}\right). \quad (2.9)$$

This is similar to Equation 2.6, but with the extra parameter gX/u^{*2} , identifying individual spectra at fixed fetch. Figure 2.6 shows observed spectra at varying fetch,

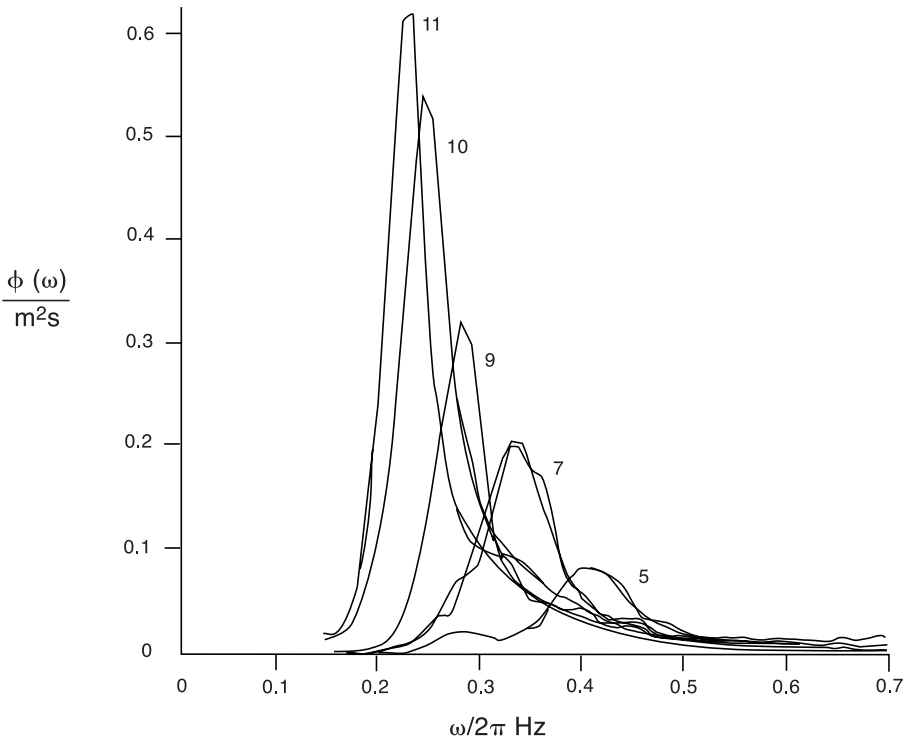


Figure 2.6 Evolution of the spectrum with increasing fetch, from 10 (label 5) to 80 (label 11) km, according to the JONSWAP observations. The labels denote successive observation platforms, the intermediate ones at 20, 37, and 52 km. From Hasselman et al. (1973).

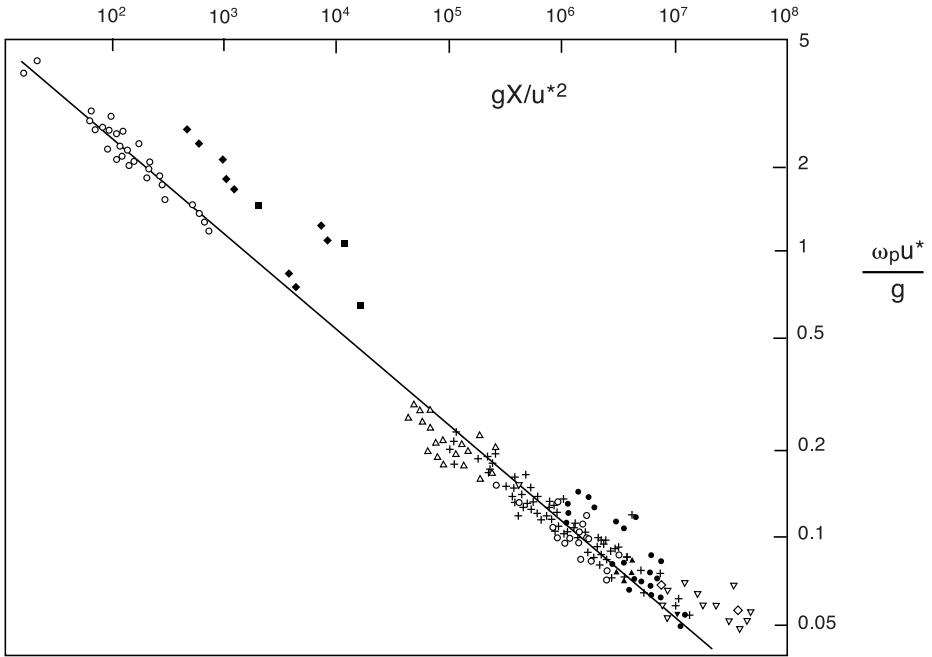


Figure 2.7 Peak frequency versus fetch in Kitagorodskii's nondimensional variables, in field and laboratory observations. From Hasselman et al. (1973).

from Hasselman et al. (1973). Although they have some common characteristics, the spectra cannot be reduced to the same shape by a rescaling of the axes. The peaks occur at lower and lower frequencies with increasing fetch, but the peaks are taller while the spreads are narrower at high than at low fetch.

The highest value of spectral density is thus a characteristic property of the wave spectrum at given fetch. At this spectral peak, the derivative of the spectral density with respect to frequency vanishes, and Equation 2.9 implies a functional relationship between nondimensional frequency at the spectral peak and nondimensional fetch:

$$\frac{u^* \omega_p}{g} = \text{func.} \left(\frac{gX}{u^{*2}} \right). \quad (2.10)$$

The particular form of this law emerged from several extensive field studies, and is, according to Hasselman et al. (1973), as shown here in Figure 2.7:

$$\frac{u^* \omega_p}{g} = 7.1 \left(\frac{gX}{u^{*2}} \right)^{-1/3}. \quad (2.11)$$

Integrating the nondimensional spectra also yields a quantity depending on nondimensional fetch alone, the nondimensional mean square elevation. Hasselman et al. (1973) gave the following empirical result:

$$\frac{g^2 \overline{\zeta^2}}{u^{*4}} = 1.6 \times 10^{-4} \frac{gX}{u^{*2}} \quad (2.12)$$

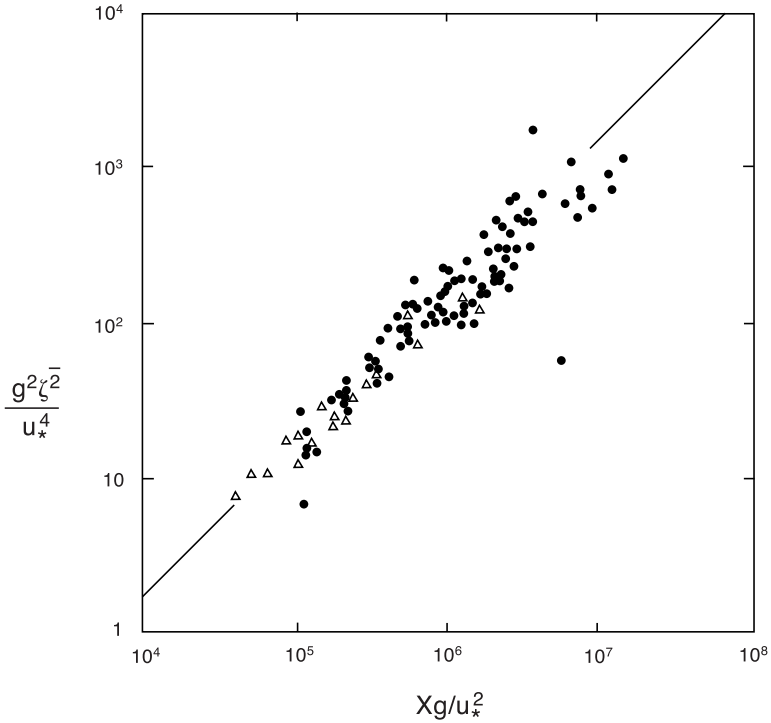


Figure 2.8 Mean square surface elevation versus fetch in nondimensional variables, from Phillips (1977).

remarkably, a linear relationship (see Figure 2.8). Eliminating the fetch from the last two equations leads to a wave-height to peak frequency relationship:

$$\frac{g\sqrt{\zeta^2}}{u^{*2}} = 0.057 \left(\frac{u^* \omega_p}{g} \right)^{-3/2}. \quad (2.13)$$

This has become known as Toba's (1972) 3/2 power law, if expressed in terms of characteristic wave period, defined as $T_p = 2\pi/\omega_p$, and significant wave height $H_s = 4\sqrt{\zeta^2}$:

$$\frac{gH_s}{u^{*2}} = 0.061 \left(\frac{gT_p}{u^*} \right)^{3/2} \quad (2.14)$$

(see Toba, 1972 and Figure 2.9).

Once the characteristic wave is long enough not to be affected by capillarity, it travels at the free gravity-wave celerity $C_p = \sqrt{g/k_p} = \omega_p/k_p$. This is true in practice on every natural surface where waves have been systematically observed. In laboratory flumes, a correction for capillarity applies. In any case, the nondimensional celerity C_p/u^* is a convenient variable to represent the stage of growth of the windsea, and has come to be known as “wave age.” From the gravity wave formula, plus Equations 2.11 and 2.12, the following set of relationships emerge, expressing key wave properties in

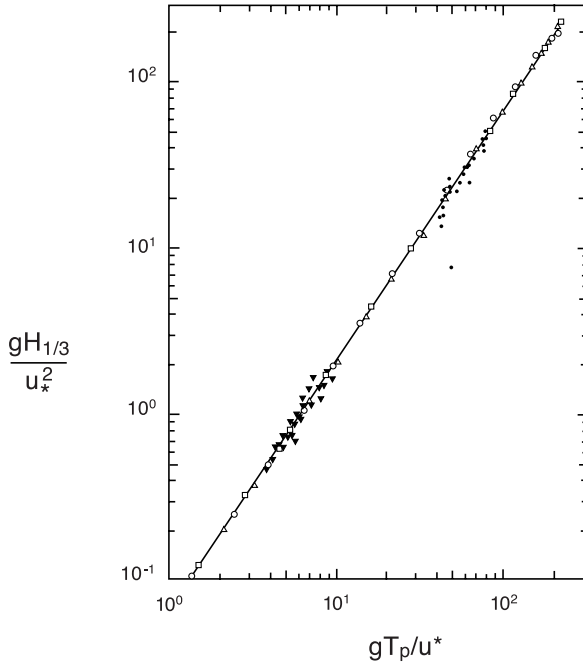


Figure 2.9 The 3/2 power law between nondimensional significant wave height and significant period. From Toba (1972).

function of wave age:

$$\begin{aligned}\frac{gX}{u_*^2} &= 358 \left(\frac{C_p}{u_*} \right)^3 \\ \frac{gH_{1/3}}{u_*^2} &= 0.96 \left(\frac{C_p}{u_*} \right)^{3/2} \\ \frac{gT_p}{u_*} &= 6.27 \frac{C_p}{u_*}.\end{aligned}\tag{2.15}$$

These give the fetch, characteristic waveheight, and wave period in function of wave age. Other wave properties of interest include steepness, one measure of which is waveheight to wavelength ratio, $H_{1/3}/\lambda_p$, where $\lambda_p = 2\pi/k_p$ is the wavelength of a gravity wave of wavenumber k_p . Equation 2.15 implies:

$$\frac{H_{1/3}}{\lambda} = 0.153 \left(\frac{C_p}{u_*} \right)^{-1/2}\tag{2.16}$$

so that characteristic wave steepness decreases with increasing wave age. The steepness of a small amplitude gravity wave, $\zeta = a \sin(\omega_p t)$, is ak_p , and its amplitude a is proportional to the root mean square elevation, $a = \sqrt{2\zeta^2}$. Using this connection to

assign an amplitude to the characteristic wave, steepness as ak_p becomes:

$$ak_p = 0.34 \left(\frac{C_p}{u^*} \right)^{-1/2}. \quad (2.17)$$

For fully developed waves these formulae give 0.0275 for the waveheight to wavelength ratio, and 0.061 for ak_p .

Particles in a small amplitude gravity wave of celerity C_p execute a residual motion called ‘‘Stokes drift,’’ because they spend slightly more time in forward than in backward motion, owing to wave propagation. The surface velocity of Stokes drift in small-amplitude, free gravity waves is $u_s = a^2 k_p^2 C_p$. The long waves of the windsea undoubtedly give rise to residual motion for the same physical reason as gravity waves, so that using the gravity wave formula for Stokes drift, with Equation 2.17 for steepness, should be a reasonable estimate. A substitution yields $u_s = 0.11u^* \cong 3.3u_w^*$, where u_w^* is the friction velocity on the water side, $u_w^* = \sqrt{\tau_i/\rho_w}$, smaller than the air-side u^* in the ratio of the square roots of densities. To the accuracy of this estimate, surface Stokes drift is independent of fetch or wave age, varying with wind stress alone.

Perhaps the most important property of waves is their transport of horizontal momentum. Small amplitude gravity waves transport momentum at the rate $M_t = \rho_w g a^2 / 4 = \rho_w g \bar{\zeta}^2 / 2$. The same formula presumably gives a realistic estimate of momentum transport by the windsea. A substitution of Equation 2.12 leads to:

$$M_t = 0.064\tau_i X \quad (2.18)$$

where τ_i is the interface shear stress.

To the accuracy of the gravity wave formulae for estimating Stokes drift and momentum transport, these results identify two invariants of wave growth under constant wind stress: the surface velocity of Stokes drift, and the divergence of momentum transport, dM_t/dX . Equation 2.18 also tells us that 6.4% of the momentum transferred from the wind to the water supports the growth of the characteristic wave, by supplying the wave momentum transport divergence. The linear growth of momentum transport with fetch comes directly from the empirical Equation 2.12, and from the gravity wave relationship of momentum transport to wave energy.

The various empirical laws governing wave growth are remarkable in their simplicity. While the functional form of the peak frequency law (Equation 2.11), and of the wave height law (Equation 2.12), follow from dimensional arguments, the power-law nature, the exponents, and the constants are all empirical and establish physical laws valid under constant wind stress and in the absence of swell, or as one might say, applying to the ‘‘perfect windsea’’ (à la perfect gas). Toba’s law (Equation 2.14) follows from the first two, or the peak frequency law follows from Toba’s law and the wave height law. The windsea properties in Equations 2.17 and 2.18 are estimates based on the hypothesis that the energy and the momentum transport of the wave field closely follow the gravity wave formulae, depending principally on the long waves.

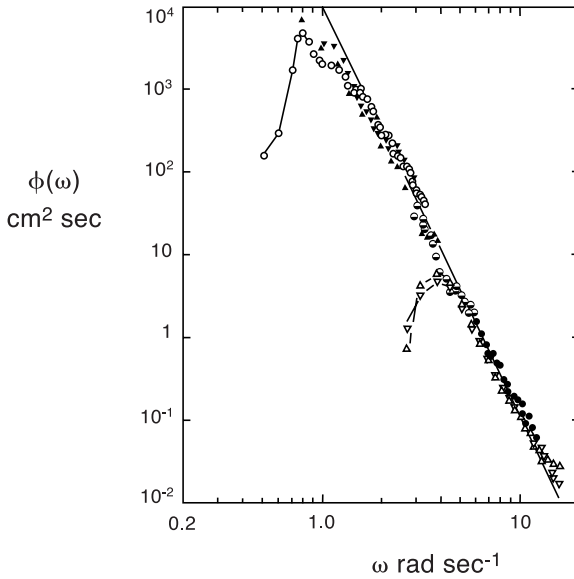


Figure 2.10 The tail of the characteristic wave at a wide range of wave ages, showing the spectral peak only in a few cases for orientation, at nondimensional fetches of $gX/u^{*2} = 5$ and 200. From Phillips (1977).

2.2.3 The Tail of the Characteristic Wave

The wind wave spectrum (Figure 2.5) shows a sharp rise ahead of ω_p , followed by a similarly sharp drop beyond, tailing off more slowly above $2\omega_p$. Remarkably, moreover, in the radian frequency range of $\omega = 1.5\text{--}12\text{ s}^{-1}$, spectra from short or long fetch, weaker or stronger winds, very nearly coincide at frequencies higher than their own ω_p , as Figure 2.10 shows, from Phillips (1977). In the log-log plot of this illustration, the data cluster around a straight line with a slope of -5. Phillips calls this the saturation range or equilibrium range of the wind wave spectrum, described by the formula:

$$\frac{\phi(\omega)\omega^5}{g^2} = \beta \quad (2.19)$$

where β is known as Phillips' constant, the constancy based on theoretical arguments.

Field observations showed, however, systematic variation of β with fetch, as Figure 2.11 here shows, taken also from Phillips (1977). A more appealing idea than some kind of equilibrium and $\beta = \text{const.}$ is to suppose that this "constant" is a function of the nondimensional peak frequency $u^*\omega_p/g$, as are all other characteristic wave properties. This then makes the frequency range in which Equation 2.19 applies, but now with $\beta = \text{func.}(u^*\omega_p/g)$, an appendage or "tail" of the characteristic wave. Physically, an interpretation is that many different realizations of the dominant waves, having different irregular shapes, heights and wavelengths, produce spectral densities in this range that depend on the characteristic frequency.

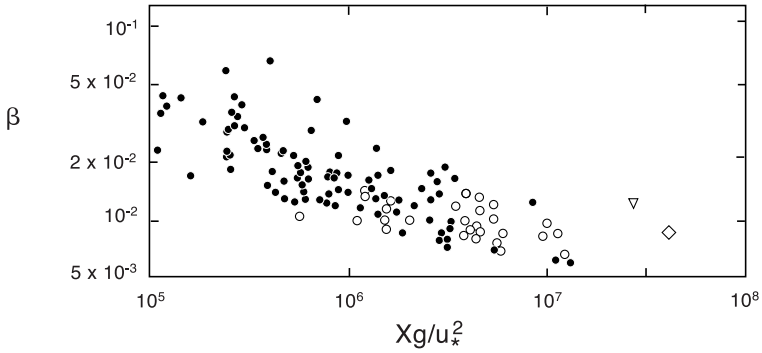


Figure 2.11 Values of the Phillips constant β from field measurements, as quoted by Phillips (1977).

If β is a function of $u^* \omega_p / g$, it is also a function of nondimensional fetch. A good match to the data in Figure 2.11 is:

$$\frac{\phi(\omega)\omega^5}{g^2} = 1.3 \left(\frac{gX}{u^{*2}} \right)^{-1/3} \quad (2.20)$$

This is equivalent to $\beta = 0.183(u^* \omega_p / g)$. The so amended Equation 2.19 conforms now to the structure of the other growth laws.

Where do all these laws come from? What physical principles underlie them? Why does wave steepness decrease while waves become higher? Why are estimated momentum transport divergence and surface Stokes drift invariant? Just as thermodynamic laws arise from the chaos of molecular agitation, so we have here macroscopic laws of wave growth arising from the interface chaos of turbulence and wind waves, laws that do not follow from established laws of fluid mechanics. A “microscopic” explanation in terms of shear flow-turbulence-wave interactions may some day be found for them, but nothing like that exists today.

The theoretical literature of wind waves is replete with attempts to find such an explanation. Most postulate energy transfer between components of the wave spectrum at different frequencies or wavenumbers. The physical basis is either a tacit or explicit assumption that spectral densities arise from freely traveling waves of frequencies ω that interact dynamically, or an analogy with Kolmogoroff’s (1941) ideas on the turbulent energy cascade, according to which energy flows from larger to smaller flow structures, with the dissipation concentrated at the high wavenumber end of the spectrum. Neither of these ideas is applicable to the windsea: Freely traveling waves differ in several important respects from wind waves, as discussed above (see Figure 2.2 and quotes from Bigelow and Edmondson, 1947). Energy dissipation in the windsea is dominated by wave breaking, and occurs at all frequencies, but most conspicuously near the peak of the spectrum on long waves. In a later section, we discuss the interesting physical process of wave breaking, a prominent feature of the windsea.

One well-known attempt at explaining wave growth in a windsea was Hasselmann's (1962, 1963 a,b) model of the evolving wind wave spectrum through nonlinear wave-to-wave energy transfer. In this model, individual spectral components behave as inviscid gravity waves, except that their spectral densities at fixed frequency change with time or fetch, owing to energy input from wind, energy dissipation, and cross-spectral transfer. Hasselmann calculated the rate of cross-spectral transfer, to or from a given frequency, from or to the rest of the spectrum, with the aid of a complex four-wave interaction theory. The model ignores the empirically well-established dependence, of just about any spectral property on the friction velocity. In a careful discussion of the Hasselmann approach, Phillips (1977) shows that the calculated nonlinear transfer rates are incompatible with the empirical growth laws.

The idea that the spectral density at *any* frequency comes from freely traveling waves, does not follow from the fact that the spectrum is the Fourier transform of the observed time series of surface elevation. In Phillips's (1977) words, the spectral density so deduced from observation may come from "the presence of higher harmonics, resulting from the coherent passage of longer waves whose crests are sharper than their troughs" – or from any other distortion of the wave shape.

The dominant waves nevertheless do travel at the wave speed of free gravity waves, as we have seen. The story of wind wave origin teaches us that, even then, they may have a structure different from free waves and behave differently (e.g., grow exponentially as instability waves). The actual, observed evolution of spectral density at fixed frequency as a function of fetch also obeys similarity laws as do other wave properties. Barnett and Sutherland (1968) compared laboratory and field observations on this windsea property, and found in both a similar rapid rise first, followed by an overshoot, then a decaying oscillation and approach to a constant spectral density attained within the tail of the characteristic wave. The initial exponential growth suggests instability waves, while the overshoot and decaying oscillation are what one finds in a damped oscillator.

Spectral components of the windsea at frequencies above ω_p do not travel at their own gravity wave speed, but at the celerity of the characteristic wave, C_p , as laboratory observations of Ramamonjariisoa (1974), quoted by Phillips (1977), have shown (Figure 2.12). Phillips remarks that the only spectral components present, at frequencies above the spectral peak, were "those associated with the deformation of the primary waves with whose speed they travel." These "do *not* [his italics] propagate as freely traveling waves . . . but are bound as harmonics of the dominant waves." Phillips adds that "in the field the range of freely traveling waves is much greater," but it is not clear that any component of the windsea can be legitimately called a freely traveling wave, prior to transformation to swell. The increasing wavelength of the characteristic wave, or the spectral density overshoot of an individual spectral component are hard to reconcile with such an idea.

A further point is that the shape of the laboratory spectrum, rescaled according to Kitagorodskii's (1973) similarity laws, is much the same as spectra from field studies.

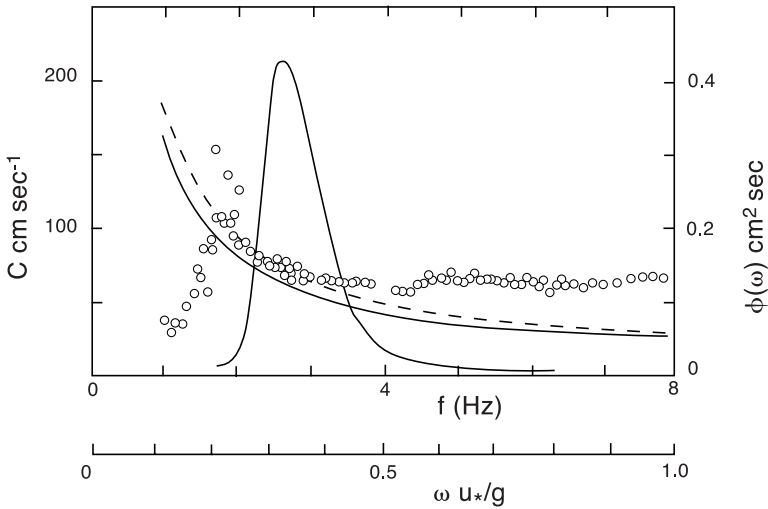


Figure 2.12 Phase speed of spectral components in a laboratory wind wave tunnel observed by Ramamonjarioa (1974), as quoted by Phillips (1977). Circles show observed phase speeds, the full and dotted lines close together free gravity wave celerities estimated in two ways, the other full line the frequency spectrum.

The term *similarity law* comes from the theory of hydrodynamic modeling: Model and prototype behave similarly; that is their laws are the same if stated in terms of Froude number or some other nondimensional variable, except for “scale effects” or “Reynolds number effects” attributable to viscosity. Laboratory waves model field waves in exactly the same way: the same nondimensional laws apply to both, including especially to the distribution of spectral densities over frequency, except for minor viscosity effects at high frequencies. What Figure 2.12 tells us about the phase speed of spectral components and how they vary with frequency should apply to the windsea after the appropriate similarity transformations.

Phillips (1977) finishes his discussion of wind wave spectrum development with the following:

“Many details are indistinct, and the parts played by the various dynamical processes involved are clearly not simple, changing constantly as the waves develop. Indeed, a dynamical kaleidoscope!”

2.2.4 Short Wind Waves

The tail of the characteristic wave extends to a radian frequency ω of about $10\text{--}12\text{ s}^{-1}$, as shown in Figure 2.10. Already at this frequency, and more so above it, spectral density is small, and makes a negligible contribution to the mean square elevation. On the other hand, the spectral density of surface *slope*, the gradient of surface elevation, $\nabla\zeta$, has its largest values at still higher frequencies. This was revealed by pioneering laboratory observations of Cox (1958), and by field observations relying on sun glitter of

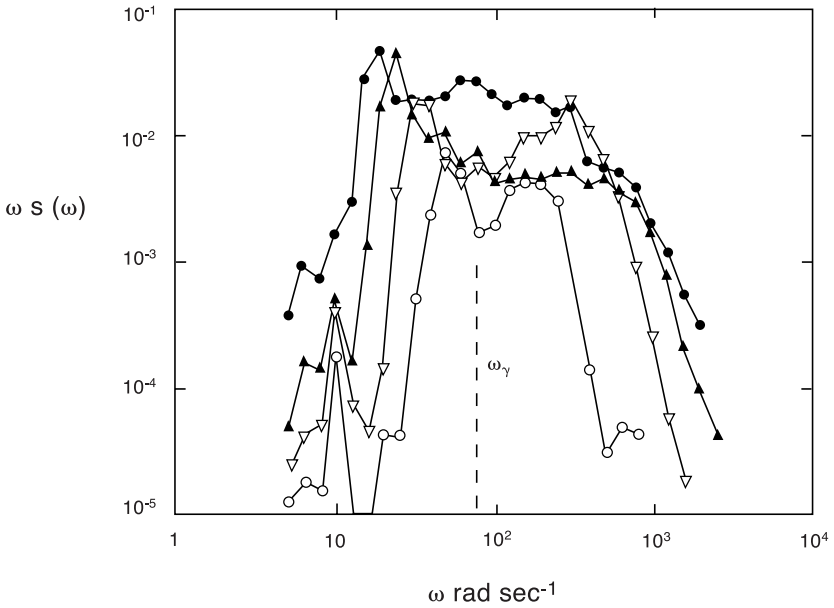


Figure 2.13 Frequency spectra of the slope of laboratory wind waves at winds varying from 3 to 12 m s⁻¹. The dotted line marks the radian frequency ω_γ that separates capillary waves from gravity waves. Data of Cox (1958), as quoted by Phillips (1977).

Cox and Munk (1954). Figure 2.13 shows Cox's laboratory data (from Phillips, 1977) on frequency-weighted slope spectral density ωS against frequency ω , with S the slope spectral density. Two striking properties of the spectra are negligible overlap with the elevation spectrum, and a nearly symmetrical distribution of frequency-weighted spectral densities around the logarithm of the frequency that separates gravity waves from capillary waves, $\omega_\gamma = (4g^3/\gamma)^{1/4}$. At this frequency, the celerity of gravity-capillary waves is a minimum. The spread around ω_γ immediately suggests that combinations of short gravity and capillary waves dominate the slope spectrum: Their presence on wind-blown natural surfaces is well-known. At any rate, the population of surface structures responsible for the slope spectrum is evidently separate from the population that produces the elevation spectrum from the characteristic wave to its tail. We will call the former population simply "short wind waves," even though they are not necessarily wave-like at all, and in nature generally three-dimensional.

Figure 2.13 also shows that both the spectral densities of surface slope, and the frequency range which they cover, increase with wind speed. So does therefore the integral of the spectrum, which is the mean square slope $(\overline{\nabla\zeta})^2$. Results of Cox and Munk (1954) derived from sun glitter on a natural wind blown surface show the increase to be approximately linear with wind speed (see Figure 2.14 and Phillips, 1977). The field data more or less agree with the laboratory observations, except at the lowest wind speed, where the laboratory mean square slope falls below a linear trend. At these short wavelengths, corresponding to the high frequency end of the spectra in Figure 2.13, scale effects resulting from viscosity may be expected.

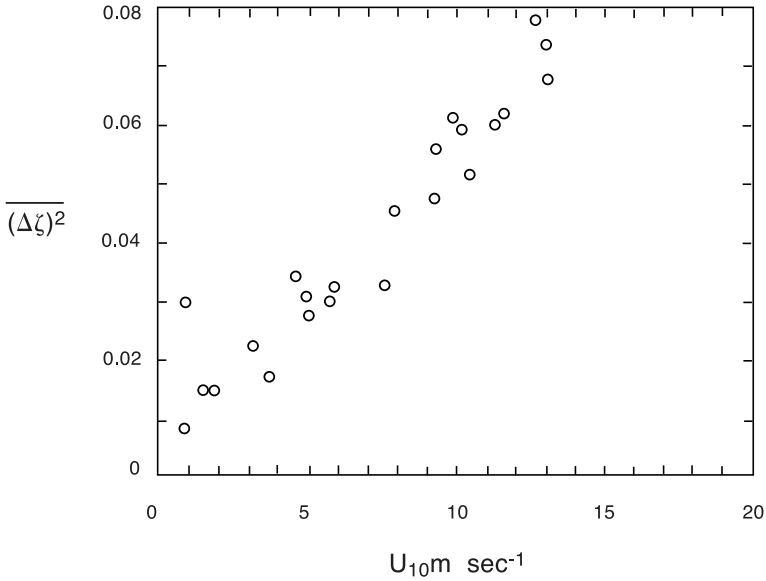


Figure 2.14 Mean square surface slope of oceanic wind waves deduced from sun glitter on a clean surface. From Cox and Munk (1954), as quoted by Phillips (1977).

Taking wind speed to be a proxy for friction velocity, the observations show that $\overline{(\nabla\zeta)^2}$ depends on u^* , as well as on the short-wave variables g , γ . A promising hypothesis is then that the mean square slope depends on those variables alone. With $\omega_\gamma = (4g^3/\gamma)^{1/4}$ a convenient proxy for surface tension, a nondimensional independent variable of familiar form is $u^*\omega_\gamma/g$. Mean square slope is already nondimensional; fitting a straight line to the data in Figure 2.14, we arrive at the relationship:

$$\overline{(\nabla\zeta)^2} = 0.017 \frac{u^*\omega_\gamma}{g} \quad (2.21)$$

a similarity law for the slope spectrum. The nondimensional spectral density ωS is a function of ω/ω_γ , in addition to $u^*\omega_\gamma/g$.

2.2.5 Laboratory Studies of Short Waves

Field observation of short waves is a particularly challenging task on account of their irregularity, not made any easier by the presence of long wind waves. Not surprisingly, systematic, quantitative field observations on short waves are far less plentiful than on long waves. We would expect laboratory studies to help out. There is a rub, however: The “short wave” range starts in the windsea near a radian frequency of $\omega = 10 \text{ s}^{-1}$, where the celerity of a gravity wave is near 1.0 m s^{-1} , its wavelength about 60 cm . Shorter wind waves on natural wind-blown surfaces are generally three-dimensional and short-lived. This is not so with wind waves in a laboratory flume. Owing to the short fetch, laboratory wind waves of order 10 cm wavelength are more or less

regular and parallel-crested, and play the role of characteristic waves. Nevertheless, laboratory observations on short wind waves have yielded a veritable treasure trove of information on how the shear flow in air and water interacts with the wave motion and the turbulence. The insights so gained helped clarify the role of short waves in air-sea transfer processes, differences between laboratory and field notwithstanding.

A whole series of pioneering observations on short wind waves have been carried out in Professor Toba's laboratory, at Tohoku University, in Sendai, Japan. That work (Toba et al., 1975; Okuda et al., 1977; Kawai, 1981, 1982; Kawamura and Toba, 1988; Yoshikawa et al., 1988; Ebuchi et al., 1993; Toba and Kawamura, 1996) provided most of the material for the following synthesis.

The short and regular initial instability waves on the laboratory air-water shear flow break down into a chaotic windsea and interior turbulence within ten seconds or so, as we discussed before. Eventually a statistically steady state of short wind waves emerges, with sharp-crested characteristic waves, similar to those visible on small lakes and ponds under moderate to strong winds. They are very "young" wind waves, of low C_p/u^* , quite steep on average; the steepness of individual dominant waves varying, however, from wave to wave.

Those variations have major effects on the air flow over the waves. In a coordinate system moving with the waves, the air flow smoothly follows the undulating surface – over waves of lesser steepness. Over some of the steeper waves, on the other hand, the air flow separates near the crest, as several careful studies have demonstrated (Banner and Peirson, 1997; Kawai, 1981, 1982; Kawamura and Toba, 1988). A "separation bubble" forms downwind of the crest, a trapped, slowly circulating air mass. A layer of strong shear separates the bubble from the free stream above, its center arching over toward the next downwind crest as Figure 2.15 illustrates (from Kawamura and Toba, 1988). The air flow reattaches again ahead of the next crest, so that the separation bubble occupies close to a full wavelength, the exact length varying from one steep wave to another. The reattaching streamlines bend upward fairly sharply where they reach the water surface, as may be seen in a photograph from Banner and Peirson (1997).

Superimposed on the above mean flow pattern is a system of large eddies attached to the waves and of wavelength dimensions, spanning the entire shear flow boundary

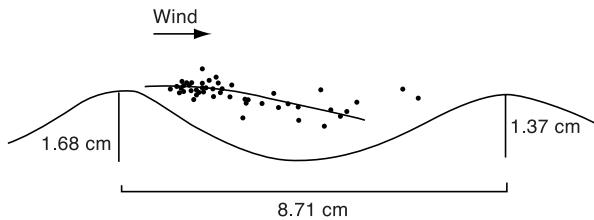


Figure 2.15 Location of high shear layer at the outer edge of the separation bubble on a steep laboratory wind wave, detected by Kawamura and Toba (1988).

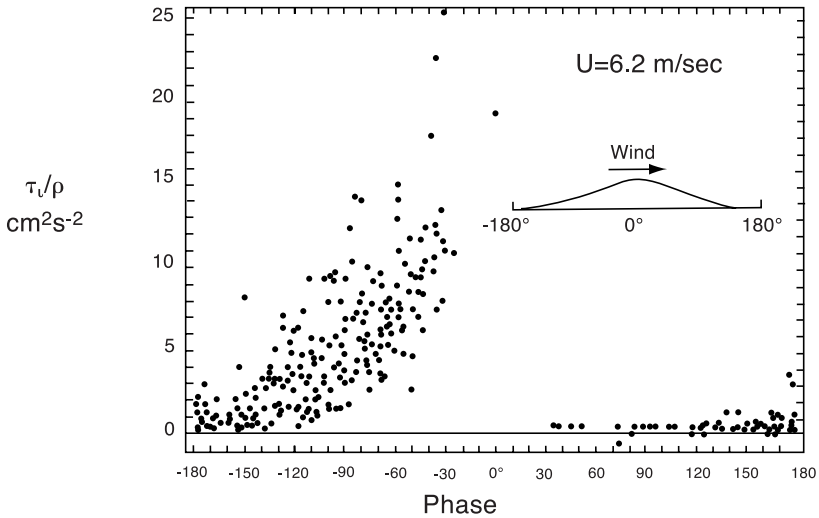


Figure 2.16 Interface shear stress distribution on laboratory wind waves, reported by Okuda et al. (1977). The peak value near the crest is some five times the area-average wind stress.

layer (Kawamura and Toba, 1988). As in wall-bound boundary layers, at a fixed point the eddies generate “bursts” of slow fluid upward, alternating with “sweeps” of fast fluid downward. Over the wavy surface, however, the bursts are statistically tied to the wave crests, the sweeps to the troughs. By way of explanation, Kawamura and Toba offer the conceptual model of a separation bubble drained by the flow, when the steep wave originating it decays, an event they call a “big burst.” The slow fluid in the bubble leaves over the downwind crest, the void behind it filled by a sweep of fast fluid.

The net horizontal force exerted on the interface, driving the water or braking the air depending on your point of view, consists of viscous shear stress and pressure force acting on the inclined surfaces of the waves. The viscous shear stress is very unevenly distributed: most of it acts on the windward face of the waves, as Okuda et al. (1977) have found (Figure 2.16). In Okuda et al.’s case, the integrated shear stress force came close to accounting for the entire momentum transfer. Banner and Peirson (1997) reported a somewhat more even distribution, significant shear force also on the leeward face. Banner and Peirson (1997) furthermore determined pressures on the interface, found them high also on the windward face, and estimated the magnitude of the resultant net pressure force at 0 to 70% of the total horizontal force, the proportion increasing from low- to high-wind speeds. This leaves 30 to 100% for the shear stress force, highest in weak winds.

The flow pattern on the air side of the steeper waves explains how forces on the windward face come to be as large as they are: Where the air flow reattaches at the downwind end of a separation bubble, both shear and pressure are intense. The shear stress is high because the boundary layer is very thin near the point of reattachment, and

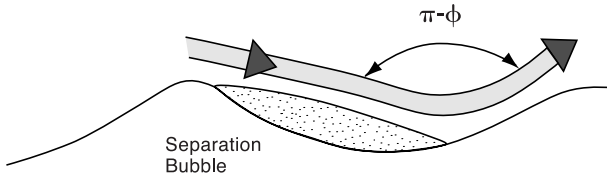


Figure 2.17 Schema of reattaching high shear layer behind a separation bubble.

the velocity outside the boundary layer is the high free stream velocity. The pressure force is high because it has to redirect the free shear layer through an angle θ .

A simple conceptual model is a two-dimensional jet (Figure 2.17), of a thickness comparable to wave amplitude a , impinging on an inclined solid surface (water being so much more massive than air, this is a good approximation). A pressure force normal to the surface deflects the jet through the angle θ , of the order of wave steepness. Acting on a wave surface inclined at a similar angle, the pressure force has a horizontal component of order $\theta^2 a U^2$ times air density, with U wind speed. The horizontal momentum transport of the air flow is diminished by this amount, in each wave with air flow separation. Divided by wave length, λ , the contribution to the resultant interface stress is of order $\theta^3 U^2$ (a/λ is of order θ). A typical value of θ for steeper laboratory waves is 0.2, so that if all waves were this steep, the drag coefficient resulting from the pressure forces alone would be $C_D = 8 \times 10^{-3}$, some four times higher than the typical observed drag.

On the water side, in the same wave-following frame of reference, the flow is upwind, counterintuitively, and also smooth under waves of low steepness. On the windward face, where the shear stress is high, a laminar boundary layer thickens and accumulates momentum deficit. The slowed down fluid shows up in pockets of vortical fluid at the crests of waves, on waves of low steepness without disorganizing the flow pattern.

On the crest of steeper waves, however, a “roller” develops from vortical fluid, a separate closed circulation, akin to, but much shorter than, the separation bubble on the air side. The presence of a roller means that the wave is “breaking,” a phenomenon discussed in detail in the next section. Breaking waves transfer much of their momentum to the shear flow. The front of the roller is steep, bore-like. The air flow separates over the roller, as several observers reported. Underneath and “downstream” (i.e., upwind) of the roller a trailing turbulent boundary layer forms on the water side of the interface, containing the momentum lost from the wave to the shear flow.

Momentum transport “crosses” the air-sea interface as shear stress and pressure force. How do interface forces on laboratory waves hand over the momentum transport to fluid motions, to reappear as Reynolds stress some distance above and below the water surface? On the air side, the upward bursts of slow air over the crests, and downward sweeps of fast air over the troughs add up to the Reynolds stress. As we have seen, the slow fluid in the bursts comes mostly from separation bubbles behind

steeper waves and separated shear layers slowed down by pressure forces. Thus, the interaction of waves with the air-side shear flow gives rise to ordered eddy motion, its length scale the wavelength, its reach the boundary layer depth. The ordered eddy motion carries the entire momentum transport, (i.e., windward momentum deficiency upward, and surplus downward.)

On the water side, any pressure force on the windward face of waves, exerted by impinging shear layers or otherwise, presses down on the free surface of a fluid in motion, (in a wave-following frame) and generates a trailing wave, by a mechanism to be discussed in connection with wave breaking. The momentum of the trailing wave combines with the momentum transport of the waves that follow. Those waves then steepen until they eventually break and lose their momentum to the water-side shear flow. This mode of momentum transfer on the water side is very different from what happens on the air side.

The water-side shear flow, sustained by viscous shear and wave breaking, transfers its momentum downward through large eddy motions coupled to the waves, similarly to the air side. Toba et al. (1975) reported “forced convection” from the crest of short waves, in the first of such laboratory studies at Tohoku University. They found that “the surface converges [ahead of] the crest, making a downward flow there.” In the light of later studies, we may place the convergence at the front of the roller on a breaking short wave. According to Ebuchi et al. (1993): “From a point close to the crest on the leeward face of individual waves, a parcel of water with high velocity (burst) goes downward through a particular route relative to the wave phase.” They showed the particular route in an illuminating illustration, (Figure 2.18): starting at the toe of the roller, the burst dives downward and backward (upwind). The compensating sweep to replace lost roller fluid is presumably less noticeable. In a further extension of the Tohoku University studies, Yoshikawa et al. (1988) and Toba and Kawamura (1996) have referred to the turbulent flow regime on the water side of the interface as the wind wave coupled “downward-bursting boundary layer.” Thus, once the momentum is in shear flow momentum, the further handover process on the water side is much as on the air side, burst and sweep phases of large eddies sustain Reynolds stress, the eddies tied to rollers, therefore moving with the steeper waves. The difference

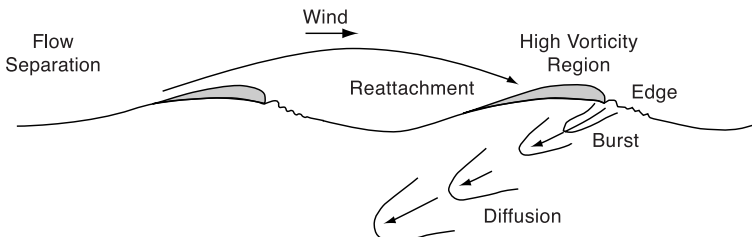


Figure 2.18 Interacting dominant flow features above and below the air-water interface illustrating: reattaching air flow, roller (“high vorticity region”) on the wave crest, downward burst at roller toe, capillaries in front. From Ebuchi et al. (1993).

is at the start of this route: Pressure forces causing waves to steepen and break, and hand over momentum downward. How exactly this happens is the subject of the next section.

2.3 The Breaking of Waves

From the growth laws, we inferred that just 6% or so of the wind-imparted momentum supports the increase of wave momentum transport with fetch. A further share of the wind input must replace wave momentum continually lost and transferred to the water-side shear flow via various dissipative processes. The most important such process is wave breaking, a more or less violent overturning motion, made conspicuous by a multitude of whitecaps, particularly numerous in strong winds. Foam makes whitecaps white, air bubbles form the foam, and the overturning motion traps the bubbles. Not all waves are breakers, however, and not all breakers trap enough air bubbles to carry whitecaps. The physics of wave breaking remained obscure until quite recently, when a combination of field, laboratory, and theoretical studies elucidated its essentials.

Waves “break” when some fluid particles on their surface, usually near the wave crest, travel faster than the wave, overtaking it. From the point of view of an observer traveling with the wave, the fast particles still travel forward in the direction of wave motion, while slower particles move backward. If the motion in this frame of reference is steady, its streamlines have a stagnation point on the surface where the forward motion begins, and another such point where it ends. The streamline connecting the stagnation points forms the boundary of a separate closed circulation cell, known as a “roller;” a pocket of fluid moving with the wave. It is usually located near and slightly ahead of the wave crest (Figure 2.19). The roller may be a boiling, churning mass of water, as in the “plunging” breakers often seen on beaches. At the other extreme, no more than a sharp crest marks the rollers on “microscale” breakers of short wavelength, often preceded by a few capillary waves. At the intermediate scale,

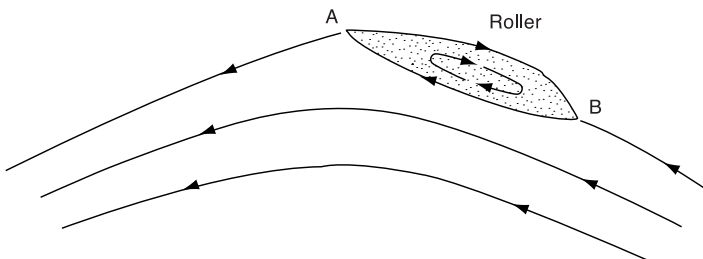


Figure 2.19 Schematic mean flow streamlines in a wave-following frame of reference near the crest of a breaking wave, showing a roller. The surface fluid travels faster than the wave (in a fixed frame of reference) between the tail A and toe B of the roller.

the “spilling” breakers of long wind waves seem to spill gently down the forward faces of the waves, from a roller ahead of the crest. Many spilling breakers are marked by whitecaps. The shape of rollers on spilling breakers resemble bores and hydraulic jumps seen on tidal rivers, in that they contain steep fronts ahead of a slightly higher surface that propagates relative to the underlying water mass. A roller similarly moves with the wave, leaving the underlying fluid behind.

The technical criterion of wave breaking is therefore $u > c$, where u is fluid particle velocity somewhere on the wave surface, and c is wave celerity. In a seminal paper, Banner and Melville (1976) pointed out that this criterion not only implies the presence of a roller, but also a separation bubble, the roller’s twin on the air side of the interface. Because air and water molecules stick together at the interface, the stagnation points on the water surface are also stagnation points for the air flow, in the wave-following frame of reference.

Under what circumstances can we expect surface particle velocity in wind waves to exceed celerity? In the absence of wind, on a mechanically generated gravity wave, the maximum particle velocity is of order $u = akc$, steepness ak times celerity. At given celerity, gravity waves break at a critical steepness. Wind stress generates surface shear flow in the water in addition to waves, increasing surface velocities. Wind waves therefore break at lower steepness than gravity waves (Banner and Phillips, 1974). On the growing waves of the windsea, at given wind stress and fetch, both the surface shear flow and the steepness of the characteristic wave are fixed, and so is therefore the average propensity of long waves to breaking. Under such conditions, in a population of long wind waves, a certain fraction are steep enough to break. According to the similarity laws, that fraction should depend on wave age.

What happens to a wave when it breaks? Just as breakers on a beach, those far from shore lose some of their energy, ending up after breaking with lower waveheight and momentum transport, and a lot of turbulence. Loss of momentum transport by the wave implies momentum transfer to the shear flow, loss of wave height, and energy transfer to shear flow and turbulence. The mechanism of the momentum transfer, a puzzle until recently, has turned out to be particularly interesting.

2.3.1 Momentum Transfer in a Breaking Wave

Two classic memoirs of Duncan (1981, 1983) elucidated that mechanism, reporting on his laboratory experiments. Figure 2.20 illustrates his apparatus: laboratory flume and a towed hydrofoil, spanning the flume. A quasi-steady breaking wave appeared behind the hydrofoil “when the foil speed, angle of attack and depth of submergence were adjusted properly.” The angle of attack of the hydrofoil was either 5° or 10° , in which configuration the hydrofoil exerted a strong downward force on the water. This force, moving forward with the hydrofoil at twelve different towing speeds between 0.62 and 1.03 m s^{-1} , left a wave behind, steep enough to break, and to carry a roller in a more or less steady formation. The first larger breaking wave was followed by a smaller amplitude trailing wave train. In a frame of reference moving with the hydrofoil, the

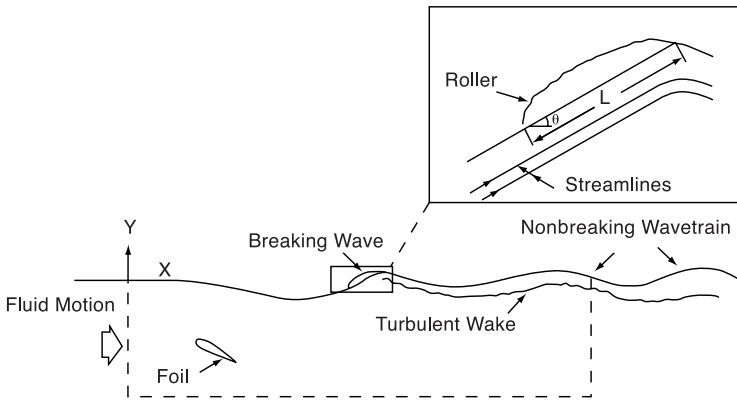


Figure 2.20 Duncan's (1981) apparatus for the study of quasi-steady breaking waves and following wave train, with details of the roller (inset) and control volume for momentum balances (broken line).

waves were stationary, while the fluid streamed by in the direction opposite to the hydrofoil's motion. The flow behind the hydrofoil thus simulated conditions along and behind a breaker on the ocean surface. Duncan's observations determined overall momentum balances, as well as the roller-wave interaction.

First, the overall momentum balances. Duncan (1981, 1983) calculated these for control volumes sketched into Figure 2.20. The undisturbed flow (in a frame of reference moving with the hydrofoil) ahead of the hydrofoil carried no waves, so that its momentum transport was simply the vertical integral of density times approach velocity, equal in magnitude to the hydrofoil velocity. Behind the hydrofoil, but ahead of the roller, the momentum transport was less by the horizontal force on the hydrofoil per unit width of the flume, the hydrofoil's so-called "wave-making resistance." In the absence of breaking, a trailing wave train moving with the hydrofoil would carry all this momentum upstream as wave momentum transport. With a breaker present, there was still a trailing wave train behind the breaker, but of smaller amplitude, as well as a turbulent "wake" (i.e., surface shear flow slowed down by the breaker). The total momentum deficit was the same before and behind the breaker, but behind the breaker it consisted of the upstream wave momentum transport of the trailing wave train, plus the momentum transport deficit in the trailing turbulent wake.

The wake started under the roller, and slowly grew in thickness with distance behind. Its growth rate was the same as of other turbulent wakes behind immersed obstacles, while its momentum transport deficit remained constant, and could be calculated from observation. That deficit had to come from a shear force that the roller exerted on the fluid stream underneath it, analogously to the resistance force of any immersed object. The turbulent wake analogy was confirmed in full detail by observations of Battjes and Sakai (1981). Furthermore, dye injection in Duncan's experiments visually demonstrated the physical presence of a turbulent wake, growing in depth "downstream" (i.e., with distance behind the hydrofoil). The important point for the physics of wave

breaking is that loss of wave momentum transport in the breaker equaled wake momentum gain behind, revealing the breaker to be an instrument of “wave to wake” momentum transport conversion.

For the purpose of determining roller-wave interaction, it is necessary to regard the roller as a two-dimensional body of fluid separate from the rest of the wave motion below. This is a conceptual model of only the mean motion, superimposed on which there is vigorous turbulence, exchanging fluid between the roller and the underlying flow, and sustaining a Reynolds stress. That stress, integrated over the bottom of the roller, adds up to a shear force equaling the momentum deficit of the trailing turbulent wake. Duncan could not rigorously assign a boundary separating roller and wave motion: he approximated it by a straight sloping line, of length L , from the observed rear stagnation point (in the wave-following frame) to an apparent toe (see the insert in Figure 2.20). The length L , and the inclination angle θ against the horizontal of the supposed bottom of the roller, were the important empirical shape parameters of the roller needed in the dynamical analysis.

Pressure as well as shear forces act on roller bottom, the Reynolds stress being quite high: in a similar experiment Battjes and Sakai (1981) found it peaking at a value of $\overline{u'w'} = 0.01U^2$, where U is flow velocity relative to the hydrofoil or to the roller. The net force on the roller in its quasi-steady observed state has to vanish; the vertical and horizontal force balances are therefore:

$$\begin{aligned} W &= \tau L \sin(\theta) + pL \cos(\theta) \\ \tau L \cos(\theta) - pL \sin(\theta) &= 0 \end{aligned} \tag{2.22}$$

where W is the weight per spanwise width of the roller, τ and p are shear stress and pressure along roller bottom. The shear stress force τL generates the wake, and its horizontal component, $\tau L \cos(\theta)$, equals the observed momentum transport deficit of the wake. The same integrated shear force component, acting on the roller, balances the horizontal pressure force on the inclined bottom. For this balance to hold, the roller must sit on the forward face of the breaking wave, as it is observed to do, $\theta > 0$.

Eliminating the pressure terms from Equation 2.22, we find $W \sin(\theta) = \tau L$, tying the weight of the roller to the shear force determined from the trailing wake. This should be the roller’s cross-sectional area shown in Figure 2.20, times the specific gravity of the fluid, times the acceleration of gravity. To match the shear force, the specific gravity of the fluid in the roller had to be 0.61, much less than 1.0, the specific gravity of water. Duncan attributed the difference to bubbles in the roller. This is unlikely to be the full explanation. Alternative possibilities are that the actual roller bottom was above its supposed location, so that the actual roller area (and weight) was less than estimated, or that the effective value of θ was less than estimated.

The angle θ that represents the average slope of the roller bottom was always small. If we eliminate the shear force terms from Equation 2.22, we find $W \cos(\theta) = pL$, the pressure force balancing most of the weight. This indeed is the essence of the separate roller conceptual model, the weight of fluid external to the wave motion pressing

down on the fluid stream underneath the separation streamline. The inclination of that streamline against the horizontal ensures the presence of a horizontal pressure force component, that balances the shear force while diminishing wave momentum transport.

According to the momentum balances, the momentum loss of a breaking wave equals the shear force on the roller, τL . As in similar turbulent flow problems, the shear stress is likely to vary with the square of the velocity difference between roller and the fluid below, equal to wave celerity c . If we take Battjes and Sakai's (1981) laboratory value for the drag coefficient, we have the momentum loss per breaking wave of $M_d = 0.01\rho c^2 L$. Roller length is certainly less than a quarter wave, let us say $L = 0.3k_1^{-1}$. Dividing the momentum loss per breaker by wavelength we get the following rate of momentum loss per unit area:

$$\frac{M_d}{\lambda} = \frac{0.003\rho c^2}{2\pi} \cong 5.10^{-4}\rho c^2. \quad (2.23)$$

At long fetch we may put $c = U$, the wind speed. According to this result, if all waves were breakers, the total downward momentum transfer via wave breaking would be about a quarter of the wind stress, given a typical drag coefficient of $C_D = 2.10^{-3}$. Our estimates here are very "soft," however, and all we can conclude is that the breakers handle a significant fraction of the total downward momentum transfer.

The weight of the roller pressing on the surface has other effects. According to classical hydrodynamics, pressure acting on the surface of flowing water generates waves. Lamb (1957) discusses this phenomenon in detail and develops its linear theory for small disturbances. The theory shows that a concentrated force on the surface induces a gravity wave train downstream of its point of application, as well as a capillary wave train upstream. Lamb quotes the effect of a fishing line as a practical illustration, described by Russell in a delightful passage:

"When a small obstacle, such as a fishing line, is moved forward slowly through still water, or (which of course comes to the same thing) is held stationary in moving water, the surface is covered with a beautiful wave-pattern, fixed relatively to the obstacle. On the up-stream side the wave-length is short, and as Thomson [Lord Kelvin] has shown, the force governing the vibrations is principally cohesion. On the down-stream side the waves are longer and are governed principally by gravity. Both sets of waves move with the same velocity relatively to the water; namely that required in order that they may maintain a fixed position relatively to the obstacle."

For cohesion, read surface tension. The two kinds of waves having the same velocity as the moving water, $c = u$, have wavenumbers, k , satisfying the classical dispersion relationship we wrote down earlier in this chapter (Equation 2.3):

$$\gamma k^2 - u^2 k + g = 0. \quad (2.24)$$

The two roots of this equation, at $u > 0.4 \text{ m s}^{-1}$ are, to a good approximation $k_2 = u^2/\gamma$ and $k_1 = g/u^2$, characterizing capillary and gravity waves, respectively. The value of γ is near $8 \times 10^{-5} \text{ m}^3 \text{ s}^{-2}$, so that wavenumbers of capillary waves are

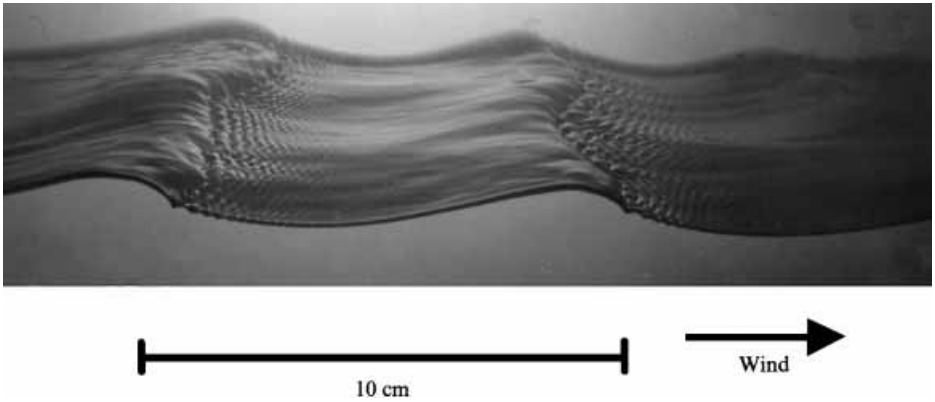


Figure 2.21 Photograph of laboratory wind wave at a fetch of 6 m, under a wind of 5.75 m s^{-1} , from Kawamura and Toba (1988). The wave shape is well-defined on the front window of the laboratory flume, the roller is marked by minor irregularities on the surface of the crest, the capillaries in front revealing the “fishing line” effect of the roller.

extremely high at celerities equal to those of long gravity waves at even moderately long fetch. Viscosity eliminates such very short capillaries, so that the upstream capillary waves of the fishing-line problem are only observable when they accompany short gravity waves, with a typical wavelength of $\lambda = 0.1 \text{ m}$, or so.

Lamb (1957) gives formulae for calculating surface elevation upstream and downstream of a concentrated vertical force acting on the surface. For gravity waves with celerities of order 10 m s^{-1} , carrying a realistic size roller, the calculated downstream effect of the roller weight is negligible, compared with the effect of the horizontal force on the inclined wave surface. On short waves, however, calculations show that a typical roller generates at least upstream capillary-gravity waves of noticeable amplitude.

At the short wavelengths of laboratory wind waves, a few capillary waves should survive elimination by viscosity. They should therefore be visible at very short fetch on natural wind-blown surfaces, as well as in laboratory flumes. They are indeed commonly observed. A particularly clear illustration of a laboratory roller with capillaries ahead is a photograph by Kawamura and Toba (1988), Figure 2.21 here. The roller shape is distinct on the transparent wall of the flume, its surface ruffled by eddy motion underneath. Visible capillaries extend to some 10 wavelengths in front.

2.4 Mechanisms of Scalar Property Transfer

The ultimate objective of this chapter is to demonstrate how wind waves facilitate the transfer of scalar properties and momentum across the air-sea interface. The preceding sections elucidated many details of the different transfer processes, and the role of wind waves in them. A synthesis is now needed, with the focus on how properties “cross

the interface,” rather than on waves or their interaction with the shear flow. Because the problem of scalar transfer is simpler, we start with its discussion.

Scalar properties, heat, water vapor, or carbon dioxide cross the air-sea interface via molecular conduction or diffusion. Molecular transport on its own is a slow process, however, as we have seen in the previous chapter. The resistance to transfer is proportional to rapidly growing thermal or diffusion-boundary layer thickness, and the square root of diffusivity. The lesser diffusivity, on the air or water side, controls the transfer rate. Wind waves and turbulence greatly diminish the resistance as they “feed” molecular diffusion, and hold diffusive boundary layer thicknesses small. Examination of this interplay reveals that the shortest flow structures are most effective in facilitating transfer. The interaction of the smallest eddies and the shortest waves with molecular diffusion, on the side of the lesser diffusivity, then controls the transfer rate.

An important distinction between the two sides arises from the high density ratio of water to air, owing to the boundary condition that air and water molecules stick together at the interface. The much more massive water slows down this motion, to the point where the interface appears almost like a solid surface to the air-side eddies, preventing significant eddy motion within the interface. By contrast, the air side is almost like vacuum to the water-side eddies, so that along-interface eddy motion is unhindered. This difference affects the way eddies and molecular diffusion cooperate in scalar transfer.

2.4.1 Water-side Resistance

How does the eddy-molecular diffusion interplay work? First we will discuss the water side, where the answer is fairly clear. The water side controls the transfer of gases of low diffusivity, as we have seen. The chemical engineering literature of gas transfer contains many attempts to elucidate the mechanism responsible. One intuitive idea due to Higbie (1935), and elaborated on by Danckwerts (1951), was “surface renewal.” This supposes that eddies bring fluid from the interior to the surface, there expose it for a limited time to a gas constituent of the air-side, and then whisk it back into the interior again. Such a model yields the same transfer coefficient as molecular diffusion on its own, but integrated over “exposure time.” The exposure time remained an arbitrary quantity: it could be deduced from observed transfer rates, but then it was simply a proxy for an empirical mass transfer velocity. Furthermore, the idea of a fluid parcel being moved from the interior to the surface conflicts with the kinematics of a fluid continuum. By definition, macroscopic parcels of fluid do not move *relative* to a free surface in the *normal* direction, only tangentially, within the interface. Spray and bubbles have their own interface that is subject to the same condition.

On account of its intuitive appeal, the surface renewal idea remains popular to this day. This in spite of Fortescue and Pearson’s (1967) clear explanation many years ago of the role of eddies in scalar transfer. They noted that a “knowledge of the kinematics of any flow field should allow the mass transport to be deducible from it,

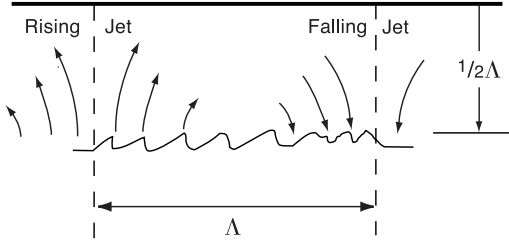


Figure 2.22 Fortescue and Pearson's (1967) schema of advection-diffusion interplay in air-sea gas transfer: Surface divergence coupled to upward moving jets keeps boundary layers thin, convergence and downward jets remove boundary layer fluid.

using standard mass conservation equations and boundary conditions.” The difficulty lies in characterizing the kinematics of eddies. As a sample eddy field, Fortescue and Pearson prescribed a row of two-dimensional circulation cells at the surface, of a characteristic size Λ , velocity scale u , and numerically solved the advection-diffusion equation to find the water to air gas transfer rates. Their principal result was that fluid rising toward the interface holds the diffusion boundary layer relatively thin, the gas transfer rate relatively high. Continuity of the fluid motions dictates that the fluid rises toward the interface in those portions of the cells where the along-interface flow is divergent. Fluid returning to the interior, where flow is convergent, takes down fluid enriched in gas. Fortescue and Pearson (1967) found the gas transfer coefficient to be a constant times $\sqrt{uD/\Lambda}$, where D is the gas diffusivity in water. The fraction u/Λ is a measure of the surface flow divergence.

The important kinematic features of Fortescue and Pearson's flow field are the divergences and convergences at the surface, above rising and sinking fluid respectively (Figure 2.22). Perhaps the simplest flow pattern with surface divergence is two-dimensional stagnation point flow, described by the streamfunction (Csanady, 1990a):

$$\psi = axz. \quad (2.25)$$

Near a stagnation point on the surface $z = 0$, at $x = 0$, the velocities are $u = ax$, $w = -az$. The constant a is the divergence of the along-surface flow, du/dx . The vertical velocity at a given depth is the same at all distances from the center of the divergence. This can only apply over a limited area, the area of the rising jet in Figure 2.22, outside of which there must be a convergence somewhere. In this idealized flow field, the steady-state advection-diffusion equation for a substance present in concentration χ is:

$$u \frac{\partial \chi}{\partial x} + w \frac{\partial \chi}{\partial z} = D \nabla^2 \chi \quad (2.26)$$

with D molecular diffusivity. The surface concentration of some gas in the water, χ_0 , in equilibrium with the gas concentration on the air-side, set by Henry's law, (discussed in section 1.7, see Equation 1.76) drives the downward diffusive flux of the gas, while advection by the rising fluid balances it. The solution of Equation 2.26 expressing this

balance is:

$$\chi = \chi_0 \operatorname{erfc} \left(z \sqrt{\frac{a}{2D}} \right). \quad (2.27)$$

The mass transfer rate or surface flux F_0 is:

$$F_0 = -k_m \chi_0 \quad (2.28)$$

where the mass transfer velocity is $k_m = \sqrt{2aD/\pi}$, a formula of the same structure as Fortescue and Pearson's (1967) result, with $a = u/\Lambda$. (The index m is necessary to distinguish mass transfer velocity from wavenumber k .) Note that both concentration and flux are independent of x , a result only valid within some effective radius of the divergent flow region. The stagnation point flow field provides the divergence, molecular agitation the diffusivity, the two together determining the transfer rate.

A similar result is likely to apply in other flow fields, with the divergence determined by the ratio of velocity and length scales of the eddy motion near the surface. As the dependence of k_m on $\Lambda^{-1/2}$ shows, the shortest length scales are likely to dominate. Comparing the result here with the molecular diffusion example in Chapter 1, we see that the surface divergence acts as a reciprocal time scale of boundary layer growth. Or, in terms of the surface renewal model, a is reciprocal exposure time.

How large are the surface divergences on the water side, in a field of wind waves? Different divergences accompany motions of different scales, long waves, short waves, eddies tied to waves, and rollers. Gravity wave divergences are of order $a_w k^2 c = a_w k \sqrt{gk} = 0.34 g^{1/4} k^{3/4} u^{*1/2}$, with their steepness $a_w k$ taken from Equation 2.17. We have written a_w for wave amplitude here, to distinguish it from divergence a . The shortest gravity waves have the largest divergences. At the short end of the gravity wave range their divergence is of order 1 s^{-1} .

Much larger divergences characterize capillary-gravity waves and rollers on short waves. What we might call a characteristic gravity-capillary wave, of frequency ω_γ , with all the steepness of short waves concentrated in it (a certain overestimate, $a_w k = \sqrt{2\nabla \xi^2}$) has a surface divergence in moderate winds of order 30 s^{-1} . Rollers on short waves originate from the rolling-up of the surface shear layer, with a vorticity of u_w^{*2}/ν_w , which is of order 100 s^{-1} in moderate winds. Surface divergence at roller fronts is of the same order.

The leading divergence producer on the water side is then the roller, with its divergence of order u_w^{*2}/ν_w . Substituting this estimate for the divergence in our formula following Equation 2.28, we arrive at:

$$k_m = \text{const. } u_w^* Sc^{-1/2} \quad (2.29)$$

with $Sc = \nu_w/D$, the Schmidt number. This applies to the neighborhood of a single roller generated surface divergence; if the area-density of such divergences, the fraction of the sea surface that they occupy, is φ , then φ times the above is the area-average transfer coefficient. The nondimensional version of this, $k^+ = k_m/u_w^*$, should then be

proportional to the area-density of roller divergences, at a fixed value of the Schmidt number.

The gas transfer law derived from observation in the moderate wind speed range is of this form, with k^+ increasing roughly linearly with u_w^* or with mean square surface slope $\overline{\nabla\zeta^2}$, according to Jähne et al. (1987), (see the last section of Chapter 1). We may now interpret the increase as being the result of the area-density of roller divergences increasing with wind speed.

According to Equation 2.21 u_ω^* and $\overline{\nabla\zeta^2}$ are linearly related. Substituting the definition of ω_γ , their relationship is:

$$\overline{\nabla\zeta^2} = 0.017\sqrt{2}\frac{u_w^*}{(g\gamma)^{1/4}}. \quad (2.30)$$

The right-hand side contains the fourth root of the waveheight scale u_w^{*2}/g to surface tension scale γ/u_w^{*2} ratio. According to the evidence, in moderate winds, this ratio is proportional to the area-density of divergences most effective in facilitating air-sea gas transfer. A reasonable conclusion to draw is that short, sharp crested waves, also known as microscale breakers, harbor the divergences that keep the diffusion boundary layer thin on a wind-blown water surface.

The simple argument above elucidating the mechanism of gas transfer in moderate winds rests on the hypothesis that the effective divergence controlling the process is proportional to the vorticity of the surface shear flow on the water side. Accumulations of viscous boundary layer fluid in microscale breakers are the suspected divergence producers as they “roll up” into rollers. The area density of microscale breakers is then the variable controlling gas transfer as well as wave steepness.

In very light winds, surface contamination affects gas transfer, while in strong winds bubbles on breakers and spray enhance gas transfer. Current and future research efforts should elucidate the extent of the enhancement.

2.4.2 Air-side Resistance

Gas transfer is the only significant scalar transfer process controlled by the water side. The air side, with its low conductivity and vapor diffusivity, controls the important heat and vapor fluxes. A major difference compared to gas transfer is that the Prandtl number for heat transfer, and the Schmidt number for vapor transfer, are of order one: Conductivity and vapor diffusivity are of the order of kinematic viscosity. Thus, any boundary layers, for temperature, vapor concentration, or shear flow are of similar thickness. The solid surface-like behavior of the water surface, suppressing significant air-side eddy motions along the interface, interposes a viscous boundary layer between the surface and any divergent flow above, and enhances the effect of the conductive or diffusive boundary layer in impeding heat and vapor transfer. The temperature or humidity difference across the viscous cum diffusive boundary layer then constitutes a significant, but not a dominant, part of the total between the surface and a reference level in the constant flux layer. Dividing this difference by the temperature or humidity flux

yields a boundary layer contribution to Resistance. Its reciprocal is a transfer velocity across the boundary layer alone. Heat transfer or evaporation therefore depends on the air-side heat conductivity or vapor diffusivity, as well as on viscosity and the waveheight length scale u_a^{*2}/g , which is also the scale of the smallest eddies.

Thicker air-side viscous cum conductive or diffusive boundary layer notwithstanding, the divergences of smallest spatial scale remain the principal conveyors of cold or dry air from above. To calculate their effects, we employ the analog of the stagnation point flow on the water side. Supposing the interface to behave as a solid surface on the air side, this is two-dimensional Hiemenz flow (Schlichting, 1960), a stagnation point flow with a viscous boundary layer. Its structure follows from boundary layer theory, and yields the mass transfer velocity across the viscous cum diffusive boundary layer (Csanady 1990a):

$$k_m = \beta \sqrt{a D_v} \quad (2.31)$$

where β is a function of Schmidt number $Sc = \nu_a/D_v$, D_v diffusivity of water vapor in air, and a is the divergence above the boundary layer. The boundary layer thickness is $\delta = \sqrt{u_a^* D_v/g}$. The heat transfer velocity is the same as k_m , with Prandtl number replacing Schmidt number, thermometric conductivity replacing diffusivity. The value of β is of order one, effectively constant.

The smallest eddies on the air side have the dimensions of short waves, with velocity scales u_a^* , length scales u_a^{*2}/g , so that the typical divergence is $a = u_a^*/(u_a^{*2}/g) = g/u_a^*$. The nondimensional transfer coefficient across the boundary layer is then:

$$k^+ = k_m/u_a^* = \beta \sqrt{\frac{g D_v}{u_a^{*3}}} \quad (2.32)$$

where $u_a^{*3}/g D_v$ is Sc^{-1} times the air-side Keulegan number, the waveheight scale to viscous length scale ratio. This implies a rapid decrease of k^+ with increasing friction velocity. The decrease in vapor concentration across a viscous-diffusive boundary layer of thickness δ , expressed as specific humidity, is then, $\Delta q = q_s - q(\delta)$:

$$\Delta q = q^*/k^+ = \beta^{-1} q^* \sqrt{\frac{u_a^{*3}}{g D_v}} \quad (2.33)$$

which is a quantity of order $10q^*$ in moderate winds with q^* the humidity flux scale introduced in Chapter 1, $q^* = \overline{\omega'q'}/u_a$.

Again as on the water side, the result in Equation 2.32 applies to a single divergence. Multiplying by area-density ϕ we have the area-average transfer coefficient across the boundary layer. In moderate to strong winds short waves cover most of the sea surface, so that the divergences that they cause have a high area-density, ϕ lose to 1.0.

Above the boundary layer, in the constant flux layer, humidity decreases further, with the logarithm of distance above the interface, as we discussed in Chapter 1. The humidity Flux-Force relationship written as a nondimensional mass transfer velocity

is $k^+ = -\overline{w'q'}/\{u_a^*[q(h) - q_s]\}$. Writing $q^* = -\overline{w'q'}/u_a^*$, the reciprocal of this can be split into $(k^+)^{-1} = [q(h) - q(\delta)]/q^* + [q(\delta) - q_s]/q^*$, the boundary layer Resistance plus a constant flux layer Resistance.

In Chapter 1 we found for the total Resistance to vapor transfer, (Equation 1.69):

$$\frac{1}{k^+} = C_s + \kappa^{-1} \ln \left(\frac{gh}{u_a^{*2}} \right) + \kappa^{-1} \ln \left(\frac{u_a^{*3}}{gD_v} \right)^{4/3} \quad (2.34)$$

again split into two parts: the first part depending on turbulence properties in the constant flux layer, and the second part on the same nondimensional parameter as appears in Equation 2.33, the ratio of waveheight length scale to diffusive boundary layer thickness, that governs the boundary layer Resistance. Equations 2.33 and 2.34 give two different versions of how this boundary layer/wind wave interaction affects vapor flux. Resistance to heat transfer behaves similarly. More important than the difference between them is that they both identify the same key nondimensional variable governing the boundary layer influence. More cannot be expected from simple models of surface divergence.

2.5 Pathways of Air-Sea Momentum Transfer

Momentum transfer differs from scalar property transfer because some of it occurs via pressure forces on the inclined surfaces of wind waves. The windsea contains two differently behaving populations of waves, one long, one short. Pressure forces generally add windward momentum to waves, long or short, increasing their momentum transport. Breaking of waves is the mechanism of transferring this momentum downward. Short waves have small amplitudes and they communicate their momentum to a shallow surface layer. Breaking long waves affect a deeper section of the oceanic mixed layer. As well as a pressure force, the airflow exerts a viscous shear force on the interface, although in a very irregular pattern, vanishing shear stress in air flow separation bubbles, high shear where shear layers reattach. We may think of these three, short waves, long waves and shear stress, as different pathways of momentum transfer “crossing” the interface, uniting again above and below into a single one of importance, the Reynolds flux of momentum (Figure 2.23). An important question on the mechanism of air-sea momentum transfer is: How wide are the individual paths?

First, momentum transfer to “long” waves. This means dominant waves of randomly varying shape, responsible for the elevation spectrum from characteristic wave to its tail. As we have seen, a constant fraction of about 6% of the wind-imparted momentum supports the increase of wave momentum transport by the windsea during wave growth from very young to mature waves. An additional fraction must balance loss of wave momentum through viscous and eddy friction plus wave breaking. Viscous friction contributes very little: The attenuation coefficient of a freely traveling classical wave is $\beta = 2\nu k^2$, yielding a half-life of the order of a year for a long wave of 60 m

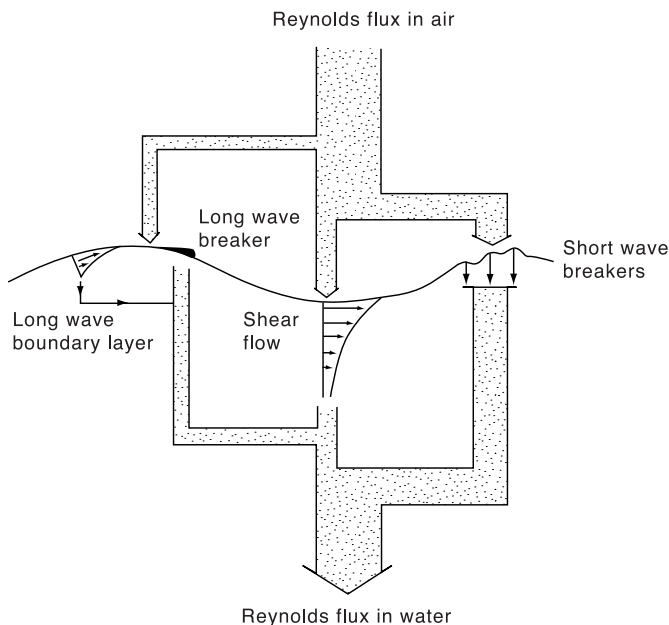


Figure 2.23 The three pathways of momentum flux crossing the air-sea interface: short waves, long waves, and viscous shear stress.

wavelength. Eddy friction on orbital motions is more effective but is still unlikely to be a significant addition to momentum transfer via wave breaking. With a typical eddy viscosity of $1 \text{ cm}^2 \text{ s}^{-1}$ in the surface layer, the half life of the same long wave is still numbered in days, or many times the wave period of 6 s. By contrast, a single breaking event transfers a large fraction of a wave's momentum downward. The dominant loss mechanism in long waves is thus wave breaking.

The details we have discussed before: the rollers on long waves and their whitecaps travel with wave celerity and their turbulence transfers momentum downward via Reynolds stress. Celerity times downward momentum transfer adds up to energy transfer. Laboratory studies on short waves showed the details of downward momentum transfer: “forced convection” from roller front down, and, in a windsea with many rollers, a “downward bursting boundary layer” on the water side of the interface. As these are inertial phenomena, they are also likely to occur on long waves. If they do, on the fast moving rollers of long waves, then long wave breaking puts much Turbulent Kinetic Energy (TKE) into the water-side mixed layer. The forced convection should reach to depths of the order of waveheight.

Recent work on water-side turbulence in the windsea (Agrawal et al., 1992; Drennan et al., 1996; Terray et al., 1996) revealed that TKE dissipation associated with long wave breaking greatly exceeds TKE production and dissipation associated with the water-side shear flow. Figure 2.24 from Drennan et al. (1996) shows nondimensional energy dissipation rate $\varepsilon H_s / F$, where F is an estimate of energy input to waves, H_s the significant waveheight, versus nondimensional depth. Considering the great difficulty

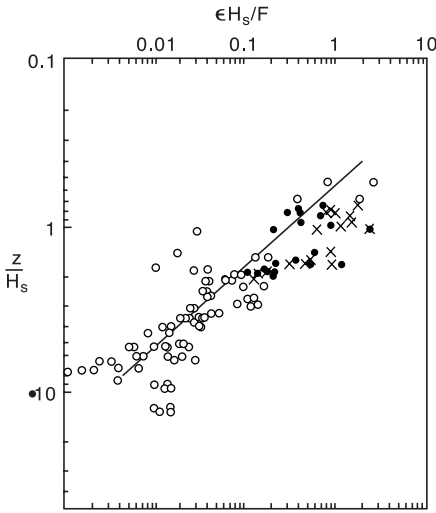


Figure 2.24 TKE dissipation rate versus depth on the water side of the interface, scaled by characteristic wave height H_s and energy input to long waves F . From Drennan et al. (1996).

of such observations in a windsea, the points line up with a clear trend. At depths comparable to wave heights, the observed dissipation rate is up to 100 times higher than what water-side shear flow generated turbulence would have produced.

These data on dissipation allow us to estimate the fraction of wind-imparted momentum that goes into long waves, traveling with a celerity close to that of the characteristic wave, C_p . Let that fraction be η , so that the momentum transfer to long waves per unit area is $\eta \rho u_w^{*2}$, the downward energy transfer C_p times that. The rest of the wind-imparted momentum goes to shear stress and short waves; these we lump together, and suppose them transmitted to the water-side shear flow, at a surface velocity of U_s . The total energy input to long waves and shear flow then equals the energy dissipation in the water-side mixed layer:

$$\eta u_w^{*2} C_p + (1 - \eta) u_w^{*2} U_s = \int_{-h}^0 \varepsilon dz. \quad (2.35)$$

Here $\varepsilon = u_w^{*3} / \kappa z + \varepsilon_L$, energy dissipation of the shear flow, plus the long wave-related dissipation ε_L . The latter dominates, and the shear flow portion may be neglected in a first approximation. On the left-hand side $C_p \gg U_s$, so that unless η is very small, its value is nearly:

$$\eta = \frac{\int_{-h}^0 \varepsilon_L dz}{u_w^{*2} C_p}. \quad (2.36)$$

Drennan et al. (1996) give the empirical formula for dissipation as $\varepsilon H_s / F = 0.3(z/H)^{-2}$. Integrating upward to the near-surface depth of about $0.5H_s$, to which the observations were limited, yields $0.6F$ for the dissipation rate integral. The dissipation rate above that level could hardly have been less than the maximum observed, or about $3F/H$, the integral $1.5F$, for a total of $2.1F$. The estimated energy input to the long waves was apparently low by a factor of two.

In one of the observed cases listed by Drennan et al. (1996), Run 18-09, using their estimated energy input and other listed data, the fraction of momentum going into long waves, $\eta = F/(u_w^{*2}C_p)$, was 21.3%. Multiplying by a factor of 2.1 brings this close to 50%. The ubiquitous presence of whitecaps on a windsea in moderate to strong winds certainly suggests that a substantial fraction of air-sea momentum transfer goes through the long wave pathway. High water-side TKE dissipation puts this expectation beyond a shadow of doubt.

Short waves include instability waves arising spontaneously under gusts of wind that intensify the shear flow. These very short waves (in the capillary-gravity wavelength range) grow and steepen rapidly, extracting momentum from the air-side boundary layer, until they break and transfer their momentum to the water-side shear flow. Similarly ephemeral are decimeter scale bore-like structures with steep fronts, as well as crescent shaped, sharp crested, wave-like surface disturbances of similar size; they also pop up and vanish in seconds, as casual observation shows. This very short time-scale activity stirs up a surface layer of a few cm in depth, as is easily demonstrated by dropping dye on the surface: it diffuses rapidly over a surface layer. Because of their ephemeral nature, it is stretching a point to say that such surface structures acquire wave momentum transport from the wind to promptly transfer it to shear flow. A bore-like structure, for example, may be driven by the pressure force of the wind on its rear, while the bore exerts an equal shear force on the fluid below, in the manner of a roller. What is common to these structures is that they extract momentum from the air flow in excess of what the mean shear would transfer over a smooth surface, much as roughness elements of a solid surface do. Short waves and other flow structures travel slowly, however, at speeds comparable to the surface velocity of the water-side shear flow, so that their contribution to downward TKE transfer is relatively small. This justifies lumping them together with viscous shear in Equation 2.35.

Properties of the slope spectrum suggest that momentum transfer via short waves could be a function of surface tension, in addition to u^* and g , and therefore could depend on the nondimensional variable $u^*\omega_\gamma/g$. In our survey of the momentum transfer laws, we did not find direct evidence for such dependence (the area-density of divergences controlling gas transfer depended, however on this variable). This seems to point the finger at the longer wavelengths in the short wave spectrum, perhaps the 0.1 to 0.3 m wavelength range, as those most effective in momentum transfer. The laboratory studies of short waves cover exactly this range, and they amply demonstrate the likely role of such waves in momentum transfer.

The laboratory evidence is not quantitatively transferable to the more diverse and chaotic short waves on the windsea. Therefore, we do not have a direct estimate of what fraction of momentum transfer passes through the short wave pathway in the open ocean: It must be the fraction left after accounting for long waves and mean viscous shear stress.

Viscous momentum transfer via the air-water shear flow remains an unavoidable corollary of the boundary conditions requiring continuous velocity and shear stress across the interface, even when breaking waves and associated flow separation

disrupt the flow pattern. Laboratory work suggests especially intense viscous momentum transfer in locations where the air flow has a downward component, such as on the downwind face of wind waves and in regions of flow reattachment behind any separation bubbles. Whatever the details, a portion of the total momentum transfer therefore remains garden variety viscous stress.

What that portion is cannot be estimated with confidence, but it should be of the order of the shear stress on a smooth wall. In the moderate wind speed range of $7\text{--}10\text{ m s}^{-1}$ Charnock's law predicts a drag coefficient about twice that of a smooth wall, suggesting that close to half of the momentum transfer may proceed via shear stress. The long waves may take another half, as we have just seen, but of course these estimates are only good within a factor of two at best. That makes all three pathways of comparable importance, the exact split unknown, but known to depend on wind speed and wave age. The arbitrary split in Figure 2.23 with a preponderance of the short wave pathway applies perhaps to young waves in moderate winds.